Three-dimensional static analysis of magneto-electro-elastic composite shells

Composite Structures 374 (2025) 119725

Contents lists available at ScienceDirect

Composite Structures

journal homepage: www.elsevier.com/locate/compstruct

Three-dimensional static analysis of magneto-electro-elastic composite shells

S. Brischetto *, D. Cesare, T. Mondino

Department of Mechanical and Aerospace Engineering, Politecnico di Torino, Torino, Italy

ARTICLE INFO

Keywords:
Smart shell structures
3D exact model
Magneto-electro-elastic coupling
Actuator configuration
Sensor configuration

ABSTRACT

The present paper is devoted to the investigation of the behavior of simply-supported multilayered smart shells embedding piezomagnetic and piezoelectric layers. A three-dimensional (3D) approach is taken into account considering the mixed curvilinear orthogonal reference system for spherical shells, cylindrical shells and cylinders. The 3D magneto-electro-elastic problem for shells is composed by a set of second order differential equations for spherical shells: the three 3D equilibrium equations, the 3D divergence equation for the magnetic induction and the 3D divergence equation for the electric displacement. The solution procedure involves the use of Navier harmonic forms in the in-plane directions and the exponential matrix method in the thickness direction. Both sensor and actuator configurations for simply supported structures can be analyzed thanks to proper load boundary impositions on external surfaces. A layer-wise approach is implemented because congruence conditions on displacements, magnetic and electric potentials and equilibrium conditions on transverse shear and transverse normal stresses, transverse normal magnetic induction and transverse normal electric displacement are imposed between two adjacent layers. In the results section, a first subsection for the validation of the present model is proposed considering comparisons with other results in literature. The proposed 3D model is more general than 3D models proposed in the literature because it uses a general formulation for several geometries, lamination schemes and load conditions. In the second subsection, new cases are shown. Tabular values and graphical trends along the thickness direction are given for different variables. These new cases can be used to investigate magneto-electro-elastic coupling, material layer and thickness layer effects on curved smart structures with different geometries and load boundary conditions. Moreover, these results can be used as references for those scientists interested in the validation of 2D/3D numerical models because the proposed 3D model is exact, layer wise and it correctly considers zigzag effects and interlaminar continuity conditions. An accurate 3D evaluation of all the elasto-electro-magnetic variables in smart structures allows a more effective design for both sensor and actuator configurations.

1. Introduction

The design of aerospace structures considering multilayered magneto-electro-elastic smart shells will be a fundamental topic in order to increase efficiency and safety of flights of the next generation of aircraft. Multilayered smart shells can be convenient as they can be used in different ways: vibration suppression during flights [1–5] or sensor and actuator applications for the structural health monitoring [6–12]. In the health monitoring applications, the magneto-electro-elastic coupling is visible because mechanical loads applied to the structure create electric and magnetic potentials in output (sensor configuration) or the electric and magnetic potentials acting on the structure create an elastic deformation (actuator configuration). Some real applications were further discussed in [13–15].

In the open literature, many scientists developed analytical and numerical plate theories to understand the static behavior of magneto-electro-elastic smart structures. Pan [16] proposed a three-dimensional (3D) exact solution for simply-supported multilayered rectangular plates under static loadings considering the Stroh formalism. The same author extended in [17] the Stroh formalism to functionally graded simply-supported rectangular plates too. Wang et al. [18] presented an analytical solution for 3D simply-supported transversely isotropic axisymmetric magneto-electro-elastic circular plates. Milazzo [19] developed a model for the large analysis of magneto-electro-elastic laminated plates considering the first order shear deformation theory and the von Karman stress function approach. In [20], Lage et al. presented a static layerwise finite element model for magneto-electro-elastic adaptive plate structures. Rao et al. [21] proposed a nonlinear finite rotation shell element for the static analysis of layered magneto-electro-elastic composite structures. In [22], a multi-physical cell-based smoothed finite element method, based on the strain smoothing technique, was

* Correspondence to: Department of Mechanical and Aerospace Engineering, Politecnico di Torino, corso Duca degli Abruzzi 24, 10129 Torino, Italy.
E-mail address: salvatore.brischetto@polito.it (S. Brischetto).

https://doi.org/10.1016/j.compstruct.2025.119725
Received 13 June 2025; Received in revised form 27 August 2025; Accepted 2 October 2025
Available online 6 October 2025

proposed to understand the hygrothermal effect on magneto-electro-elastic structures. In [23], a modified Pagano method was adopted for the 3D analysis of simply-supported functionally graded rectangular plates under magneto-electro-mechanical loads. She and He [24] investigated the thermal and post-buckling of magneto-electro-thermal-elastic plates with initial geometric defects. The nonlinear vibration equation was derived via first-order shear deformation plate theory, energy method and Galerkin methodology. Gan and She [25] coupled longitudinal and transverse excitations to investigate the combined resonance of magneto-electro-elastic plates. Maxwell equation and first order shear deformation theory were applied and Galerkin method was employed to solve the nonlinear ordinary differential equations.

Recently, the interest for numerical and analytical formulations for curved multilayered magneto-electro-elastic structures is increasing. In [26], Nixdorf and Pan presented the analytical solution of plain strain equations for anisotropic layered magneto-electro-elastic cylinders where governing equations were solved via the separation of variables and the eigenfunction expansion. An analytical solution, involving the spherical system of vector functions for the static analysis of a spherically anisotropic and multilayered magneto-electro-elastic hollow sphere, was proposed in [27]. Sobhy [28] showed an analytical formulation for the magneto-electro-thermal bending of multilayered doubly-curved shallow shells reinforced with functionally graded graphene platelets and surrounded by piezoelectromagnetic sheets. Arefi and Amabili [29] studied the 3D magneto-electro-elastic bending and buckling of three-layered doubly curved nanoshells with the nonlocal elasticity theory. Scaled boundary finite element method was used in [30] for the 3D bending analysis of laminated magneto-electro-elastic cylindrical shells under mechanical or electric/magnetic potential loads. Displacements and internal nodal forces were computed considering the state-space method and the integration technique. In [31], Monge et al. presented a polynomial layer-wise model to analyze the bending of magneto-electric shells with variable radii of curvature. A further extension, considering a non-polynomial hybrid model, was proposed in [32] for shell applications. magneto-electro-elastic doubly curved sandwich microshells subjected to multi-field static loadings were investigated by Song et al. [33] considering a new thickness stretching and including a refined higher order shear/normal deformable model. The nonlinear deflection problem of magneto-electro-elastic shells reinforced with carbon nanotubes and subjected to multiphysics loads was studied by Mahesh and Harursampath in [34] by using an higher order shell theory and von-Karman's nonlinearities. A modified shell model was developed in [35] for the buckling behavior of smart composite nanotubes under magneto-electro-elastic loads. The hybrid nanotube was composed by a carbon nanotube and a microtubule integrated with a magneto-electro-elastic layer. In Albarody et al. [36], a linear magneto-electro-elastic multilayered shell model was proposed for simply supported boundary conditions and cross-ply or anti-symmetric angle-ply lamination schemes. Tornabene et al. [37] showed a higher order formulation for the static analysis of laminated anisotropic magneto-electro-elastic doubly-curved shells. A generalized formulation based on the equivalent layer-wise approach was developed. Wu and Tsai [38] presented a work where the 3D static behavior of doubly curved functionally graded magneto-electro-elastic shells was analyzed by means of an asymptotic approach under all possible load boundary configurations (mechanical, electric and magnetic ones). A mesh-free collocation method, based on differential reproducing kernel approximations, was developed in [39] for the 3D analysis of simply-supported doubly curved functionally graded magneto-electro-elastic shells under mechanical loads and electric displacements and magnetic fluxes. Cai and She [40] used the classical theory and Maxwell equation to develop the nonlinear motion equations. The Runge–Kutta technique was adopted to determine the dynamic deflection. Influences of various factors on nonlinear dynamic response of magneto-electro-elastic cylindrical shells subjected to moving load were discussed. Gan and She [41] investigated the transient response of imperfect magneto-electro-elastic cylindrical shells under pulse load in thermal environment. Love thin shell theory and Maxwell equations were combined with Hamiltonian principle and Galerkin method to derive the nonlinear dynamic equations of cylindrical shells.

In the present paper, a 3D static shell formulation, which couples magnetic, electric and elastic fields, is proposed. The sensor and actuator behavior of simply-supported multilayered curved structures embedding piezoelectric and piezomagnetic laminae is analyzed. The mixed curvilinear orthogonal reference system allows to analyze cylinders, cylindrical panels and spherical shells considering a unique formulation thanks to a proper choice for radii of curvature. The 3D models already proposed in the literature had a significant limitation, as they were developed for specific geometries, loading conditions, and/or lamination schemes. This new 3D model is as general as possible, even if it is proposed in an exact form. Furthermore, it is developed in a layer-wise approach and with the exact calculation of derivatives in the z direction of all primary variable components, thus providing an exact 3D stress field. The 3D governing equations for the magneto-electro-elastic spherical shell problem are solved in an exact way by means of the Navier harmonic forms in the in-plane directions and the exponential matrix method in the thickness direction. This 3D exact model has a low computational cost and it is free of numerical errors and problems; therefore, it can be used as reference for validations of numerical models. Adopted 3D governing equations show each effect involved in curved multilayered smart structures, in particular thickness layer effects and transverse material anisotropy effects. In addition, the model implements the layerwise approach via interlaminar continuity conditions in terms of congruence on displacements, electric potential and magnetic potential and equilibrium on transverse shear/normal stresses, transverse normal electric displacement and transverse normal magnetic induction. In this way, the typical zigzag effect of multifield variables is recovered. One of the first works of the first author on static and pure elastic 3D analysis of shells using the exponential matrix is [42]. The first extension of this methodology to the coupled thermo-elastic analysis can be found in [43]. Further extensions to the static fully coupled electro-elastic and magneto-elastic cases are shown in [44,45], respectively. In this new paper, the analytical 3D layer-wise model for shells based on the exponential matrix method is extended for the first time to the static fully coupled electro-magneto-elastic analysis of smart curved panels. Section 2 presents the 3D governing equations for the magneto-electro-elastic spherical shell case and the related solution methodology. Section 3 is the result section, it is splitted in a preliminary validation case subsection and in a new benchmark case subsection. In both subsections, results are deeply discussed. In Section 4, main conclusions are shown. An accurate 3D evaluation of all elasto-electro-magnetic variables in layer form allows the design of a new generation of smart structures that will be more efficient and safer when used as both sensors and actuators.

2. The 3D magneto-electro-elastic shell problem

In the present section, the formulation for the 3D magneto-electro-elastic shell problem is proposed. In the first subsection, the second-order differential governing equations are presented. In the second subsection, constitutive and geometrical shell relations are discussed. Therefore, the solution methodology adopted for this problem is discussed in depth.

2.1. 3D governing shell equations

The compact form of 3D governing equations for the magneto-electro-elastic shell problem written in the mixed curvilinear orthogonal reference system (α, β, z) are: 3D equilibrium equations, a 3D divergence equation for the electric displacement and a 3D divergence

equation for the magnetic induction. Therefore, 3D governing equations for the magneto-electro-elastic shell problem can be written for spherical shells in accordance with [46–48]:

$$H_\beta(z)\frac{\partial}{\partial\alpha}\begin{Bmatrix}\sigma^k_{\alpha\alpha}\\ \sigma^k_{\alpha\beta}\\ \sigma^k_{\alpha z}\end{Bmatrix} + H_\alpha(z)\frac{\partial}{\partial\beta}\begin{Bmatrix}\sigma^k_{\alpha\beta}\\ \sigma^k_{\beta\beta}\\ \sigma^k_{\beta z}\end{Bmatrix} + H_\alpha(z)H_\beta(z)\frac{\partial}{\partial z}\begin{Bmatrix}\sigma^k_{\alpha z}\\ \sigma^k_{\beta z}\\ \sigma^k_{zz}\end{Bmatrix} + \frac{H_\beta(z)}{R_\alpha}\left(\begin{Bmatrix}\sigma^k_{\alpha z}\\ \sigma^k_{\beta z}\\ \sigma^k_{zz}\end{Bmatrix} - \begin{Bmatrix}-\sigma^k_{\alpha z}\\ 0\\ \sigma^k_{\alpha\alpha}\end{Bmatrix}\right) + \frac{H_\alpha(z)}{R_\beta}\left(\begin{Bmatrix}\sigma^k_{\alpha z}\\ \sigma^k_{\beta z}\\ \sigma^k_{zz}\end{Bmatrix} - \begin{Bmatrix}0\\ -\sigma^k_{\beta z}\\ \sigma^k_{\beta\beta}\end{Bmatrix}\right) = \begin{Bmatrix}0\\0\\0\end{Bmatrix}, \tag{1a}$$

$$\boldsymbol{\nabla}\cdot\begin{Bmatrix}\frac{1}{H_\alpha(z)}\mathcal{D}^k_\alpha\\ \frac{1}{H_\beta(z)}\mathcal{D}^k_\beta\\ \mathcal{D}^k_z\end{Bmatrix} = 0, \tag{1b}$$

$$\boldsymbol{\nabla}\cdot\begin{Bmatrix}\frac{1}{H_\alpha(z)}\mathcal{B}^k_\alpha\\ \frac{1}{H_\beta(z)}\mathcal{B}^k_\beta\\ \mathcal{B}^k_z\end{Bmatrix} = 0, \tag{1c}$$

where $\begin{Bmatrix}\sigma^k_{\alpha\alpha}\\ \sigma^k_{\alpha\beta}\\ \sigma^k_{\alpha z}\end{Bmatrix}$ is the stress component vector for stresses acting on the face perpendicular to α axis, $\begin{Bmatrix}\sigma^k_{\alpha\beta}\\ \sigma^k_{\beta\beta}\\ \sigma^k_{\beta z}\end{Bmatrix}$ is the stress component vector for stresses acting on the face perpendicular to β axis, $\begin{Bmatrix}\sigma^k_{\alpha z}\\ \sigma^k_{\beta z}\\ \sigma^k_{zz}\end{Bmatrix}$ is the stress component vector for stresses acting on the face perpendicular to z axis, $\begin{Bmatrix}-\sigma^k_{\alpha z}\\ 0\\ \sigma^k_{\alpha\alpha}\end{Bmatrix}$ is the stress component vector that considers R_α correction, $\begin{Bmatrix}0\\ -\sigma^k_{\beta z}\\ \sigma^k_{\beta\beta}\end{Bmatrix}$ is the stress component vector that considers R_β correction, $\begin{Bmatrix}\frac{1}{H_\alpha(z)}\mathcal{D}^k_\alpha\\ \frac{1}{H_\beta(z)}\mathcal{D}^k_\beta\\ \mathcal{D}^k_z\end{Bmatrix}$ is the electric displacement component vector including curvature terms and $\begin{Bmatrix}\frac{1}{H_\alpha(z)}\mathcal{B}^k_\alpha\\ \frac{1}{H_\beta(z)}\mathcal{B}^k_\beta\\ \mathcal{B}^k_z\end{Bmatrix}$ is the magnetic induction component vector including curvature terms. $\frac{\partial}{\partial\alpha}$, $\frac{\partial}{\partial\beta}$ and $\frac{\partial}{\partial z}$ are the partial derivatives in α, β and z directions, respectively. Terms $H_\alpha(z)$ and $H_\beta(z)$ are defined for shell geometries as:

$$H_\alpha(z) = 1 + z/R_\alpha, \qquad H_\beta(z) = 1 + z/R_\beta, \tag{2}$$

where R_α and R_β are radii of curvature in α and β directions, respectively. As no curvature is shown in the z direction, $H_z = 1$ because R_z radius of curvature is infinite. $\boldsymbol{\nabla}\cdot$ is the divergence operator. In order to compact the formulation, in the rest of the paper, $H_\alpha(z)$ and $H_\beta(z)$ are indicated without the explicit dependence on z. z goes from $-\frac{h}{2}$ to $+\frac{h}{2}$; $\bar{z}$ goes from 0 to h. h is the total thickness.

The set of second-order differential equations written in the mixed curvilinear reference system (α, β, z) can be properly specialized for different geometries such as cylinders, cylindrical panels and spherical shell panels considering appropriate R_α and R_β values. These two radii of curvature are computed on the Ω_0 reference surface. When R_α and R_β are infinite, terms $H_\alpha(z)$ and $H_\beta(z)$ are equal 1 and Eqs. (1) degenerate in those for plates. In Fig. 1, all the possible geometries that can be analyzed with the mixed curvilinear orthogonal reference system are shown.

2.2. Constitutive and geometrical shell relations

Constitutive relations for the 3D magneto-electro-elastic shell problem are employed to couple elastic, magnetic and electric fields as confirmed in [49]. The starting point is the classical 3D Hooke law for pure elastic problems. Constitutive equations can be written for each k layer as:

$$\boldsymbol{\sigma}^k = \boldsymbol{C}^k\boldsymbol{\varepsilon}^k - \boldsymbol{e}^{kT}\boldsymbol{\Upsilon}^k - \boldsymbol{q}^{kT}\boldsymbol{\mathcal{H}}^k, \tag{3a}$$

$$\boldsymbol{\mathcal{D}}^k = \boldsymbol{e}^k\boldsymbol{\varepsilon}^k + \boldsymbol{\epsilon}^k\boldsymbol{\Upsilon}^k + \boldsymbol{d}^k\boldsymbol{\mathcal{H}}^k, \tag{3b}$$

$$\boldsymbol{\mathcal{B}}^k = \boldsymbol{q}^k\boldsymbol{\varepsilon}^k + \boldsymbol{d}^k\boldsymbol{\Upsilon}^k + \boldsymbol{\mu}^k\boldsymbol{\mathcal{H}}^k, \tag{3c}$$

where the 6×1 stress vector is:

$$\boldsymbol{\sigma}^k = \begin{Bmatrix}\sigma^k_{\alpha\alpha}\\ \sigma^k_{\beta\beta}\\ \sigma^k_{zz}\\ \sigma^k_{\beta z}\\ \sigma^k_{\alpha z}\\ \sigma^k_{\alpha\beta}\end{Bmatrix}, \tag{4}$$

the 6×6 elastic coefficient matrix for orthotropic materials is:

$$\boldsymbol{C}^k = \begin{bmatrix} C^k_{11} & C^k_{12} & C^k_{13} & 0 & 0 & 0\\ C^k_{12} & C^k_{22} & C^k_{23} & 0 & 0 & 0\\ C^k_{13} & C^k_{23} & C^k_{33} & 0 & 0 & 0\\ 0 & 0 & 0 & C^k_{44} & 0 & 0\\ 0 & 0 & 0 & 0 & C^k_{55} & 0\\ 0 & 0 & 0 & 0 & 0 & C^k_{66}\end{bmatrix}, \tag{5}$$

the 6×1 strain vector is:

$$\boldsymbol{\varepsilon}^k = \begin{Bmatrix}\varepsilon^k_{\alpha\alpha}\\ \varepsilon^k_{\beta\beta}\\ \varepsilon^k_{zz}\\ \gamma^k_{\beta z}\\ \gamma^k_{\alpha z}\\ \gamma^k_{\alpha\beta}\end{Bmatrix}, \tag{6}$$

the 3×6 piezoelectric coefficient matrix for orthotropic materials is:

$$\boldsymbol{e}^k = \begin{bmatrix} 0 & 0 & 0 & 0 & e^k_{15} & 0\\ 0 & 0 & 0 & e^k_{24} & 0 & 0\\ e^k_{31} & e^k_{32} & e^k_{33} & 0 & 0 & 0\end{bmatrix}, \tag{7}$$

the 3×1 electric field vector is:

$$\boldsymbol{\Upsilon}^k = \begin{Bmatrix}\Upsilon^k_\alpha\\ \Upsilon^k_\beta\\ \Upsilon^k_z\end{Bmatrix}, \tag{8}$$

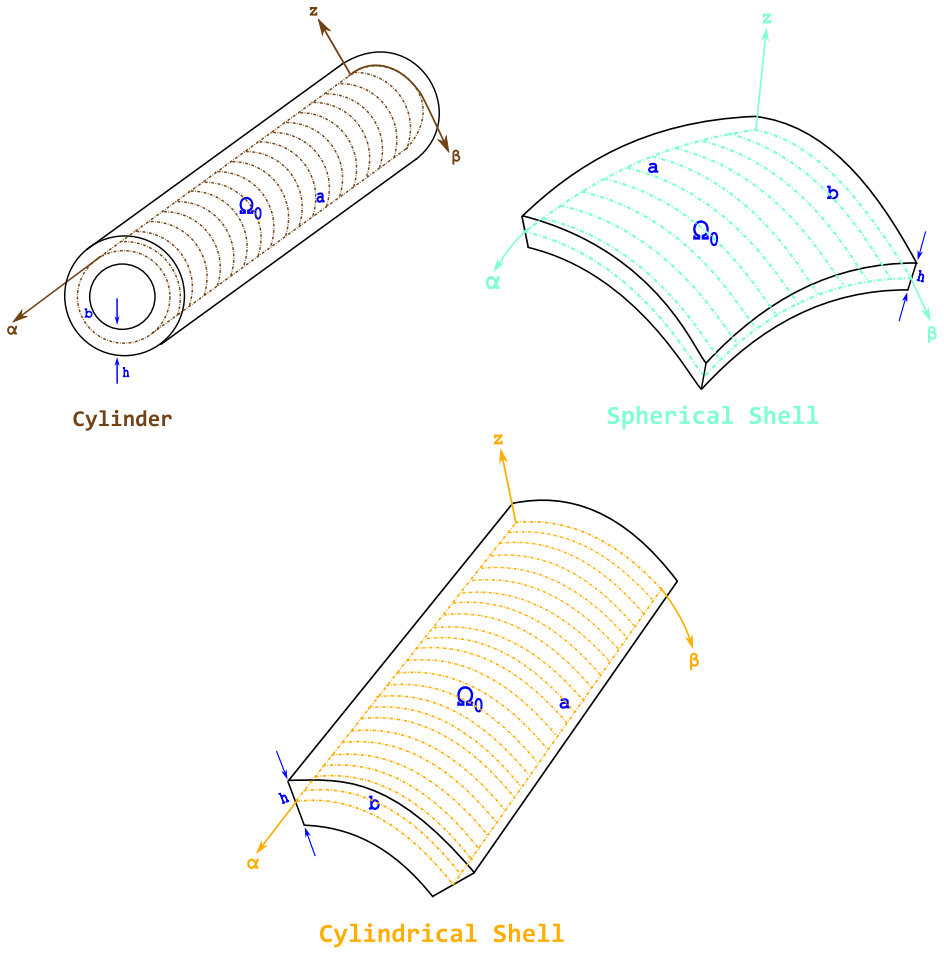

Fig. 1. Geometries, mixed curvilinear orthogonal reference system and middle reference surfaces for validation cases and new cases.

the 3×6 piezomagnetic coefficient matrix for orthotropic materials is:

$$\boldsymbol{q}^k = \begin{bmatrix} 0 & 0 & 0 & 0 & q^k_{15} & 0 \\ 0 & 0 & 0 & q^k_{24} & 0 & 0 \\ q^k_{31} & q^k_{32} & q^k_{33} & 0 & 0 & 0 \end{bmatrix}, \tag{9}$$

the 3×1 magnetic field vector is:

$$\boldsymbol{\mathcal{H}}^k = \begin{Bmatrix} \mathcal{H}^k_\alpha \\ \mathcal{H}^k_\beta \\ \mathcal{H}^k_z \end{Bmatrix}, \tag{10}$$

the 3×1 electric displacement vector is:

$$\boldsymbol{\mathcal{D}}^k = \begin{Bmatrix} \mathcal{D}^k_\alpha \\ \mathcal{D}^k_\beta \\ \mathcal{D}^k_z \end{Bmatrix}, \tag{11}$$

the 3×3 electric permittivity coefficient matrix for orthotropic materials can be written as:

$$\boldsymbol{\epsilon}^k = \begin{bmatrix} \epsilon^k_{11} & 0 & 0 \\ 0 & \epsilon^k_{22} & 0 \\ 0 & 0 & \epsilon^k_{33} \end{bmatrix}, \tag{12}$$

the 3×3 magneto-electric coupling coefficient matrix for orthotropic materials has the following form:

$$\boldsymbol{d}^k = \begin{bmatrix} d^k_{11} & 0 & 0 \\ 0 & d^k_{22} & 0 \\ 0 & 0 & d^k_{33} \end{bmatrix}, \tag{13}$$

the 3×1 magnetic induction vector is:

$$\boldsymbol{\mathcal{B}}^k = \begin{Bmatrix} \mathcal{B}^k_\alpha \\ \mathcal{B}^k_\beta \\ \mathcal{B}^k_z \end{Bmatrix}, \tag{14}$$

the 3×3 magnetic permittivity coefficient matrix for orthotropic materials has the following diagonal form:

$$\boldsymbol{\mu}^k = \begin{bmatrix} \mu^k_{11} & 0 & 0 \\ 0 & \mu^k_{22} & 0 \\ 0 & 0 & \mu^k_{33} \end{bmatrix}. \tag{15}$$

All constitutive equations (3) and related matrices and vectors are written for the 0° or 90° orthotropic lamination angle in order to have a closed form solution of the problem. Geometrical relations connect strains $\boldsymbol{\epsilon}^k$ with displacements $\boldsymbol{u}^k$ (as already seen for pure elastic problems), the magnetic field $\boldsymbol{\mathcal{H}}^k$ with the magnetic potential ψ^k and the electric field $\boldsymbol{\Upsilon}^k$ with the electric potential ϕ^k. They can be written in the (α, β, z) mixed curvilinear orthogonal reference system for spherical shells in accordance with [46–48]:

$$\boldsymbol{\epsilon}^k = \boldsymbol{\Delta}^k(z)\boldsymbol{u}^k, \tag{16a}$$

$$\boldsymbol{\mathcal{H}}^k = -\boldsymbol{\Delta}^k_{\mathcal{H}}(z)\psi^k, \tag{16b}$$

$$\boldsymbol{\Upsilon}^k = -\boldsymbol{\Delta}^k_{\Upsilon}(z)\phi^k, \tag{16c}$$

where

$\boldsymbol{u}^k = \begin{Bmatrix} u^k \\ v^k \\ w^k \end{Bmatrix}$ is the 3×1 displacement vector, and ψ^k and ϕ^k

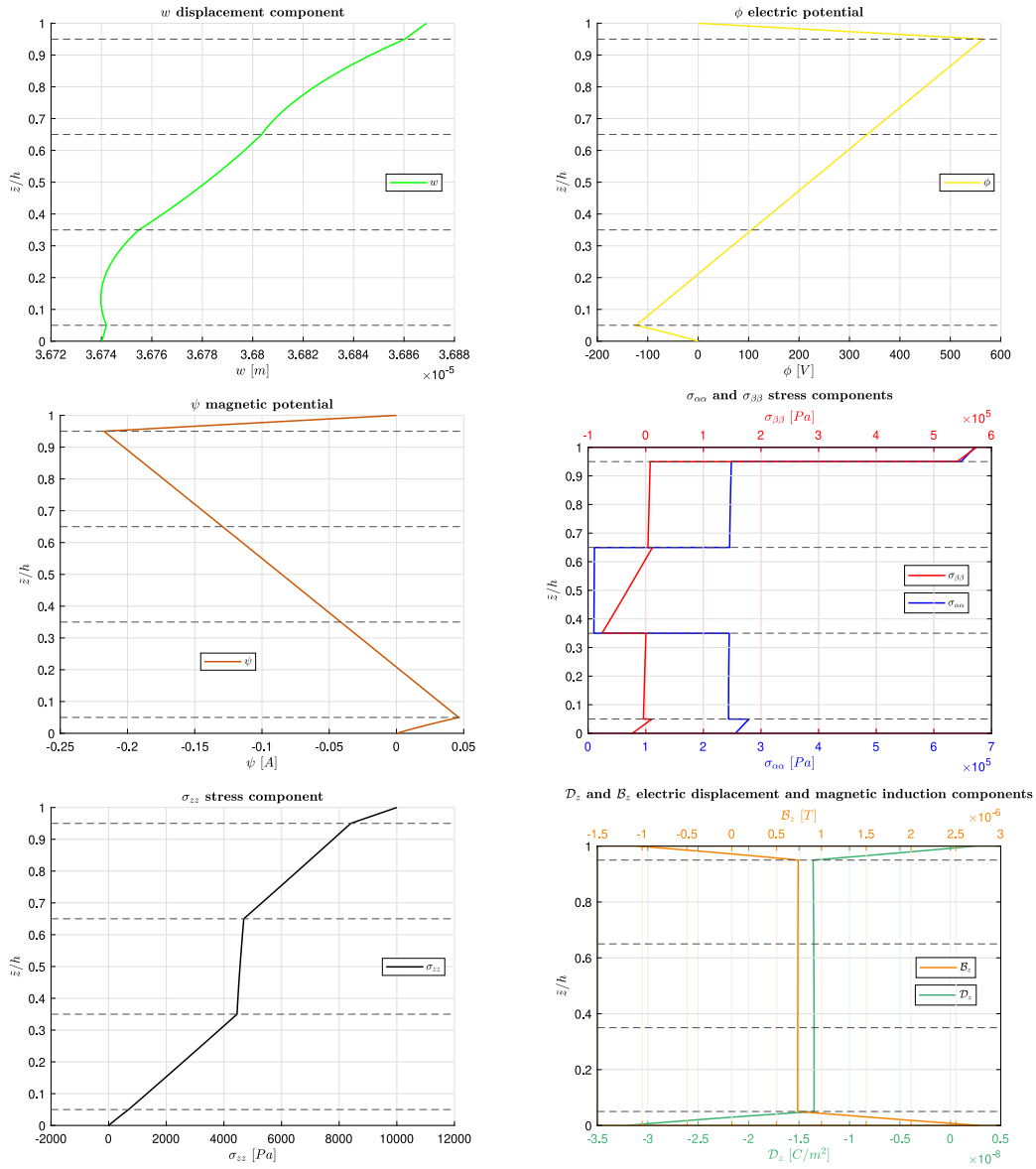

Fig. 2. First new case in sensor configuration. Simply-supported multilayered (Adaptive Wood/0°/90°/0°/Adaptive Wood) cylinder for $R_\alpha/h = 20$. $P_{z_t} = 10000\,\text{Pa}$, $P_{z_b} = 0\,\text{Pa}$, $\boldsymbol{\Phi}_t = \boldsymbol{\Phi}_b = 0\,\text{V}$, $\boldsymbol{\Psi}_t = \boldsymbol{\Psi}_b = 0\,\text{A}$. Imposed half-wave couples $m = 2$ and $n = 1$.

are scalar values,

the 6×3 derivative matrix for strains has the following form:

$$\boldsymbol{\Delta}^k(z) = \begin{bmatrix} \frac{1}{H_\alpha}\frac{\partial}{\partial\alpha} & 0 & \frac{1}{H_\alpha R_\alpha} \\ 0 & \frac{1}{H_\beta}\frac{\partial}{\partial\beta} & \frac{1}{H_\beta R_\beta} \\ 0 & 0 & \frac{\partial}{\partial z} \\ 0 & \frac{\partial}{\partial z} - \frac{1}{H_\beta R_\beta} & \frac{1}{H_\beta}\frac{\partial}{\partial\beta} \\ \frac{\partial}{\partial z} - \frac{1}{H_\alpha R_\alpha} & 0 & \frac{1}{H_\alpha}\frac{\partial}{\partial\alpha} \\ \frac{1}{H_\beta}\frac{\partial}{\partial\beta} & \frac{1}{H_\alpha}\frac{\partial}{\partial\alpha} & 0 \end{bmatrix}, \tag{17}$$

the 3×1 derivative vector for the magnetic potential can be written as:

$$\boldsymbol{\Delta}^k_{\mathcal{H}}(z) = \begin{Bmatrix} \frac{1}{H_\alpha}\frac{\partial}{\partial\alpha} \\ \frac{1}{H_\beta}\frac{\partial}{\partial\beta} \\ \frac{\partial}{\partial z} \end{Bmatrix}, \tag{18}$$

the 3×1 derivative vector for the electric potential is:

$$\boldsymbol{\Delta}^k_{\mathcal{Y}}(z) = \begin{Bmatrix} \frac{1}{H_\alpha}\frac{\partial}{\partial\alpha} \\ \frac{1}{H_\beta}\frac{\partial}{\partial\beta} \\ \frac{\partial}{\partial z} \end{Bmatrix}. \tag{19}$$

Vectors and matrices defined in Eqs. (17)–(19) degenerate in those for plates when R_α and R_β are infinite and terms $H_\alpha(z)$ and $H_\beta(z)$ are equal 1. Constitutive equations (3) and geometrical equations (16) are useful to correctly define the structural response of magneto-electro-elastic structures and to fully couple the three physical fields involved.

2.3. 3D formulation and solution methodology

In the present subsection, the complete theoretical formulation used to solve the 3D governing equations for the magneto-electro-elastic shell problem (Eqs. (1)) is shown. First of all, constitutive equations (3) and geometrical equations (16) must be included in the 3D governing

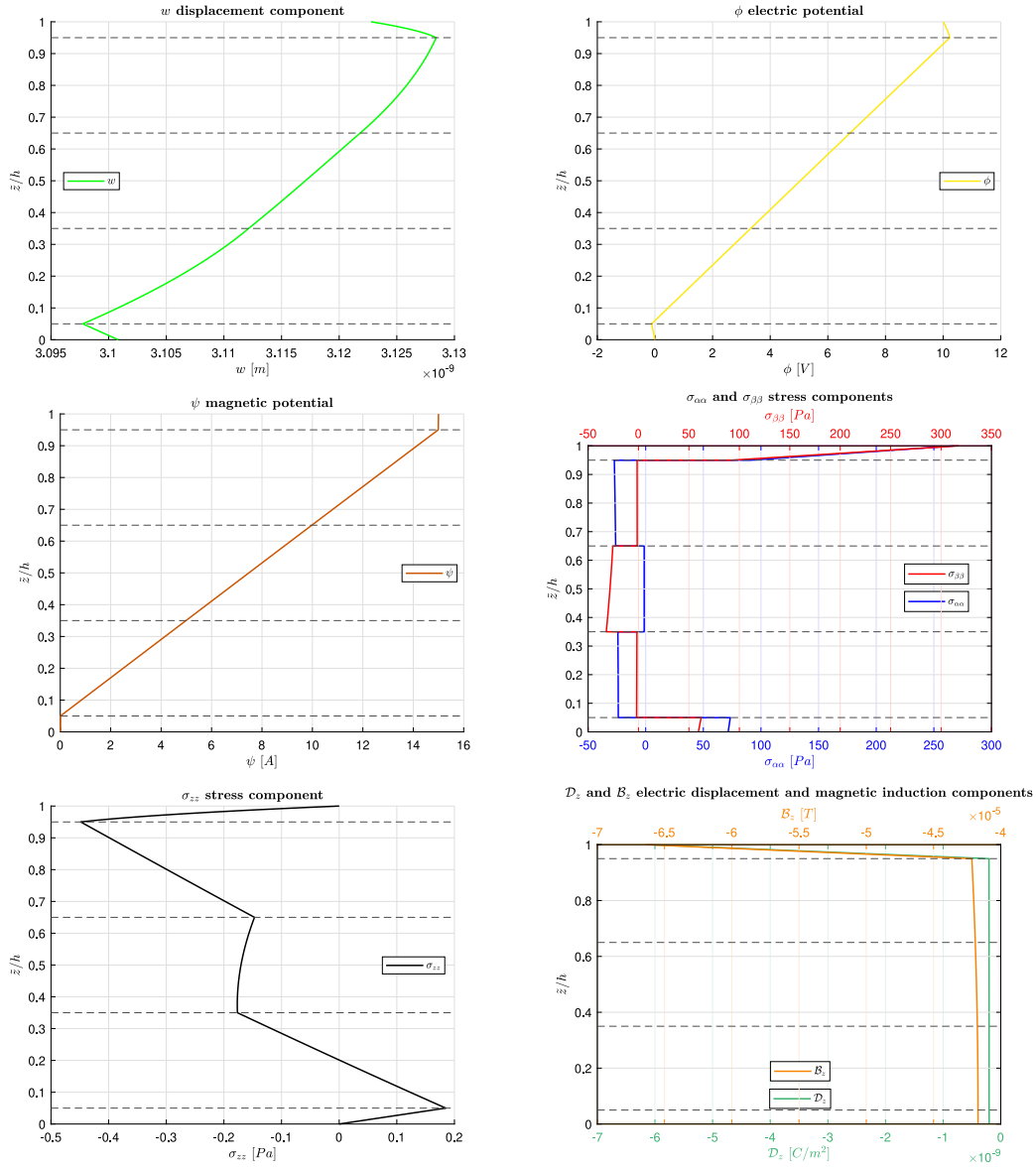

Fig. 3. First new case in actuator configuration. Simply-supported multilayered (Adaptive Wood/0°/90°/0°/Adaptive Wood) cylinder for $R_\alpha/h = 20$. $\Phi_t = 10\,\mathrm{V}$, $\Phi_b = 0\,\mathrm{V}$, $\Psi_t = 15\,\mathrm{A}$, $\Psi_b = 0\,\mathrm{A}$, $P_{z_t} = P_{z_b} = 0\,\mathrm{Pa}$. Imposed half-wave couples $m = 2$ and $n = 1$.

equations (1); in this way, Eqs. (1) are written in terms of displacements u, v and w, magnetic potential ψ and electric potential ϕ.

The solution method consists in the imposition of harmonic forms in the in-plane directions α and β. Harmonic forms automatically satisfy simply supported boundary conditions for shell sides; they are the only possibility for analytical solutions. These forms are:

$$\boldsymbol{u}^k = \begin{bmatrix} cos(\bar{\alpha}\alpha)sin(\bar{\beta}\beta) & 0 & 0 \\ 0 & sin(\bar{\alpha}\alpha)cos(\bar{\beta}\beta) & 0 \\ 0 & 0 & sin(\bar{\alpha}\alpha)sin(\bar{\beta}\beta) \end{bmatrix} \begin{Bmatrix} U^k(z) \\ V^k(z) \\ W^k(z) \end{Bmatrix}, \tag{20a}$$

$$\phi^k = \Phi^k(z)sin(\bar{\alpha}\alpha)sin(\bar{\beta}\beta), \tag{20b}$$

$$\psi^k = \Psi^k(z)sin(\bar{\alpha}\alpha)sin(\bar{\beta}\beta), \tag{20c}$$

where $U^k(z)$, $V^k(z)$, $W^k(z)$, $\Phi^k(z)$, $\Psi^k(z)$ are the amplitudes of the primary variables, and $\bar{\alpha}$ and $\bar{\beta}$ are two coefficients defined as:

$$\bar{\alpha} = \frac{m\pi}{a}, \quad \bar{\beta} = \frac{n\pi}{b}. \tag{21}$$

Terms m and n are the half-wave numbers in α and β directions, respectively. a and b are the in-plane dimensions of the structure. The substitution of harmonic forms (Eqs. (20)) in the 3D governing equations for the magneto-electro-elastic shell problem allows to perform analytically the partial derivatives in α and β:

$$\begin{aligned} &\left(-\frac{H_\beta C^k_{55}}{H_\alpha R^2_\alpha} - \frac{C^k_{55}}{R_\alpha R_\beta} - \bar{\alpha}^2\frac{C^k_{11}H_\beta}{H_\alpha} - \bar{\beta}^2\frac{C^k_{66}H_\alpha}{H_\beta}\right)U^k \\ &+ \left(-\bar{\alpha}\bar{\beta}C^k_{12} - \bar{\alpha}\bar{\beta}C^k_{66}\right)V^k + \left(\bar{\alpha}\frac{C^k_{11}H_\beta}{H_\alpha R_\alpha} + \bar{\alpha}\frac{C^k_{12}}{R_\beta} + \bar{\alpha}\frac{C^k_{55}H_\beta}{H_\alpha R_\alpha} + \bar{\alpha}\frac{C^k_{55}}{R_\beta}\right)W^k \\ &+ \left(\frac{C^k_{55}H_\beta}{R_\alpha} + \frac{C^k_{55}H_\alpha}{R_\beta}\right)U^k_{,z} + \left(\bar{\alpha}C^k_{13}H_\beta + \bar{\alpha}C^k_{55}H_\beta\right)W^k_{,z} + C^k_{55}H_\alpha H_\beta U^k_{,zz} \\ &+ \left(+2\bar{\alpha}\frac{e^k_{15}H_\beta}{H_\alpha R_\alpha} + \bar{\alpha}\frac{e^k_{15}}{R_\beta}\right)\Phi^k + \left(\bar{\alpha}e^k_{31}H_\beta + \bar{\alpha}e^k_{15}H_\beta\right)\Phi^k_{,z} \\ &+ \left(+2\bar{\alpha}\frac{q^k_{15}H_\beta}{H_\alpha R_\alpha} + \bar{\alpha}\frac{q^k_{15}}{R_\beta}\right)\Psi^k + \left(\bar{\alpha}q^k_{31}H_\beta + \bar{\alpha}q^k_{15}H_\beta\right)\Psi^k_{,z} = 0, \end{aligned} \tag{22a}$$

$$
\begin{aligned}
&\left(-\frac{H_\alpha C^k_{44}}{H_\beta R^2_\beta}-\frac{C^k_{44}}{R_\alpha R_\beta}-\bar{\alpha}^2\frac{C^k_{66}H_\beta}{H_\alpha}-\bar{\beta}^2\frac{C^k_{22}H_\alpha}{H_\beta}\right)V^k\\
&+\left(-\bar{\alpha}\bar{\beta}C^k_{12}-\bar{\alpha}\bar{\beta}C^k_{66}\right)U^k+\left(\bar{\beta}\frac{C^k_{44}H_\alpha}{H_\beta R_\beta}+\bar{\beta}\frac{C^k_{44}}{R_\alpha}+\bar{\beta}\frac{C^k_{22}H_\alpha}{H_\beta R_\beta}+\bar{\beta}\frac{C^k_{12}}{R_\alpha}\right)W^k\\
&+\left(\frac{C^k_{44}H_\alpha}{R_\beta}+\frac{C^k_{44}H_\beta}{R_\alpha}\right)V^k_{,z}+\left(\bar{\beta}C^k_{44}H_\alpha+\bar{\beta}C^k_{23}H_\alpha\right)W^k_{z}+C^k_{44}H_\alpha H_\beta V^k_{,zz}\\
&+\left(+2\bar{\beta}\frac{e^k_{24}H_\alpha}{H_\beta R_\beta}+\bar{\beta}\frac{e^k_{24}}{R_\alpha}\right)\Phi^k+\left(\bar{\beta}e^k_{32}H_\alpha+\bar{\beta}e^k_{24}H_\alpha\right)\Phi^k_{,z}\\
&+\left(+2\bar{\beta}\frac{q^k_{24}H_\alpha}{H_\beta R_\beta}+\bar{\beta}\frac{q^k_{24}}{R_\alpha}\right)\Psi^k+\left(\bar{\beta}q^k_{32}H_\alpha+\bar{\beta}q^k_{24}H_\alpha\right)\Psi^k_{,z}=0,
\end{aligned}
\tag{22b}
$$

$$
\begin{aligned}
&\left(\frac{C^k_{13}}{R_\alpha R_\beta}+\frac{C^k_{23}}{R_\alpha R_\beta}-\frac{C^k_{11}H_\beta}{H_\alpha R^2_\alpha}-\frac{2C^k_{12}}{R_\alpha R_\beta}-\frac{C^k_{22}H_\alpha}{H_\beta R^2_\beta}-\bar{\alpha}^2\frac{C^k_{55}H_\beta}{H_\alpha}-\bar{\beta}^2\frac{C^k_{44}H_\alpha}{H_\beta}\right)W^k\\
&+\left(\bar{\alpha}\frac{C^k_{55}H_\beta}{H_\alpha R_\alpha}-\bar{\alpha}\frac{C^k_{13}}{R_\beta}+\bar{\alpha}\frac{C^k_{11}H_\beta}{H_\alpha R_\alpha}+\bar{\alpha}\frac{C^k_{12}}{R_\beta}\right)U^k\\
&+\left(\bar{\beta}\frac{C^k_{44}H_\alpha}{H_\beta R_\beta}-\bar{\beta}\frac{C^k_{23}}{R_\alpha}+\bar{\beta}\frac{C^k_{22}H_\alpha}{H_\beta R_\beta}+\bar{\beta}\frac{C^k_{12}}{R_\alpha}\right)V^k\\
&+\left(-\bar{\alpha}C^k_{55}H_\beta-\bar{\alpha}C^k_{13}H_\beta\right)U^k_{,z}+\left(-\bar{\beta}C^k_{44}H_\alpha-\bar{\beta}C^k_{23}H_\alpha\right)V^k_{,z}\\
&+\left(\frac{C^k_{33}H_\beta}{R_\alpha}+\frac{C^k_{33}H_\alpha}{R_\beta}\right)W^k_{,z}\\
&+C^k_{33}H_\alpha H_\beta W^k_{,zz}+\left(-\bar{\alpha}^2\frac{e^k_{15}H_\beta}{H_\alpha}-\bar{\beta}^2\frac{e^k_{24}H_\alpha}{H_\beta}\right)\Phi^k\\
&+\left(-\bar{\alpha}^2\frac{q^k_{15}H_\beta}{H_\alpha}-\bar{\beta}^2\frac{q^k_{24}H_\alpha}{H_\beta}\right)\Psi^k\\
&+\left(-\frac{e^k_{31}H_\beta}{R_\alpha}-\frac{e^k_{32}H_\alpha}{R_\beta}+\frac{e^k_{33}H_\beta}{R_\alpha}+\frac{e^k_{33}H_\alpha}{R_\beta}\right)\Phi^k_{,z}+e^k_{33}H_\alpha H_\beta\Phi^k_{,zz}\\
&+\left(-\frac{q^k_{31}H_\beta}{R_\alpha}-\frac{q^k_{32}H_\alpha}{R_\beta}+\frac{q^k_{33}H_\beta}{R_\alpha}+\frac{q^k_{33}H_\alpha}{R_\beta}\right)\Psi^k_{,z}+q^k_{33}H_\alpha H_\beta\Psi^k_{,zz}=0,
\end{aligned}
\tag{22c}
$$

$$
\begin{aligned}
&\bar{\alpha}\frac{e^k_{15}}{H^2_\alpha R_\alpha}U^k+\bar{\beta}\frac{e^k_{24}}{H^2_\beta R_\beta}V^k+\left(-\bar{\alpha}^2\frac{e^k_{15}}{H^2_\alpha}-\bar{\beta}^2\frac{e^k_{24}}{H^2_\beta}\right)W^k\\
&+\left(-\bar{\alpha}\frac{e^k_{15}}{H_\alpha}-\bar{\alpha}\frac{e^k_{31}}{H_\alpha}\right)U^k_{,z}\\
&+\left(-\bar{\beta}\frac{e^k_{24}}{H_\beta}-\bar{\beta}\frac{e^k_{32}}{H_\beta}\right)V^k_{,z}+\left(\frac{e^k_{31}}{H_\alpha R_\alpha}+\frac{e^k_{32}}{H_\beta R_\beta}\right)W^k_{,z}+e^k_{33}W^k_{zz}\\
&+\left(\bar{\alpha}^2\frac{\epsilon^k_{11}}{H^2_\alpha}+\bar{\beta}^2\frac{\epsilon^k_{22}}{H^2_\beta}\right)\Phi^k-\epsilon^k_{33}\Phi^k_{,zz}+\left(\bar{\alpha}^2\frac{d^k_{11}}{H^2_\alpha}+\bar{\beta}^2\frac{d^k_{22}}{H^2_\beta}\right)\Psi^k-d^k_{33}\Psi^k_{,zz}=0,
\end{aligned}
\tag{22d}
$$

$$
\begin{aligned}
&\bar{\alpha}\frac{q^k_{15}}{H^2_\alpha R_\alpha}U^k+\bar{\beta}\frac{q^k_{24}}{H^2_\beta R_\beta}V^k+\left(-\bar{\alpha}^2\frac{q^k_{15}}{H^2_\alpha}-\bar{\beta}^2\frac{q^k_{24}}{H^2_\beta}\right)W^k\\
&+\left(-\bar{\alpha}\frac{q^k_{15}}{H_\alpha}-\bar{\alpha}\frac{q^k_{31}}{H_\alpha}\right)U^k_{,z}\\
&+\left(-\bar{\beta}\frac{q^k_{24}}{H_\beta}-\bar{\beta}\frac{q^k_{32}}{H_\beta}\right)V^k_{,z}+\left(\frac{q^k_{31}}{H_\alpha R_\alpha}+\frac{q^k_{32}}{H_\beta R_\beta}\right)W^k_{,z}+q^k_{33}W^k_{zz}\\
&+\left(\bar{\alpha}^2\frac{d^k_{11}}{H^2_\alpha}+\bar{\beta}^2\frac{d^k_{22}}{H^2_\beta}\right)\Phi^k-d^k_{33}\Phi^k_{,zz}+\left(\bar{\alpha}^2\frac{\mu^k_{11}}{H^2_\alpha}+\bar{\beta}^2\frac{\mu^k_{22}}{H^2_\beta}\right)\Psi^k-\mu^k_{33}\Psi^k_{,zz}=0.
\end{aligned}
\tag{22e}
$$

At this point, the unknowns of the 3D magneto-electro-elastic problem are the amplitudes of the primary variables $U(z)^k$, $V(z)^k$, $W(z)^k$, $\Phi(z)^k$, $\Psi(z)^k$ and their first and second derivatives in z. In the case of a pure elastic problem, the primary variables are $U(z)^k$, $V(z)^k$, $W(z)^k$ and related first and second derivatives in z.

In order to finalize the solution methodology, the exponential matrix method have to be implemented. This method requires two mandatory requirements: constant coefficients and a set of first-order differential equations. In order to have constant coefficients, the introduction of very thin mathematical layers, dividing each physical k layer of the multilayered structure, is adopted. So, a general j mathematical layer is introduced in the present formulation. The total number of mathematical layers is expressed with M. Equations will be written for a general j mathematical layer. No differences occur as the mathematical layers are a simple subdivision of each k physical layer. Thanks to the introduction of the mathematical layers, H_α and H_β terms can be considered as constant inside each j layer. So, coefficients of the differential equations are constant. In order to have first-order differential equations, classical redoubling procedure is performed on Eqs. (22a). This redoubling procedure includes the first derivatives in z of the unknowns as primary variables of the model. This is a huge potentiality of the exponential matrix method because these additional unknowns are fundamental to correctly compute stresses, strains, electric displacements and magnetic inductions.

The resulting set of ten first-order differential equations in z can be compacted and written in matrix form as follows:

$$
\begin{bmatrix}
A^j_{10} & 0 & 0 & 0 & 0 & 0 & 0 & 0 & 0 & 0\\
0 & A^j_{20} & 0 & 0 & 0 & 0 & 0 & 0 & 0 & 0\\
0 & 0 & P^j_1 & 0 & 0 & 0 & 0 & 0 & 0 & 0\\
0 & 0 & 0 & P^j_1 & 0 & 0 & 0 & 0 & 0 & 0\\
0 & 0 & 0 & 0 & P^j_1 & 0 & 0 & 0 & 0 & 0\\
0 & 0 & 0 & 0 & 0 & A^j_{10} & 0 & 0 & 0 & 0\\
0 & 0 & 0 & 0 & 0 & 0 & A^j_{20} & 0 & 0 & 0\\
0 & 0 & 0 & 0 & 0 & 0 & 0 & P^j_1 & 0 & 0\\
0 & 0 & 0 & 0 & 0 & 0 & 0 & 0 & P^j_1 & 0\\
0 & 0 & 0 & 0 & 0 & 0 & 0 & 0 & 0 & P^j_1
\end{bmatrix}
\begin{Bmatrix}
U^j\\ V^j\\ W^j\\ \Phi^j\\ \Psi^j\\ U^j_{,z}\\ V^j_{,z}\\ W^j_{,z}\\ \Phi^j_{,z}\\ \Psi^j_{,z}
\end{Bmatrix}_{,z}
=
$$

$$
\begin{bmatrix}
0 & 0 & 0 & 0 & 0 & A^j_{10} & 0 & 0 & 0 & 0\\
0 & 0 & 0 & 0 & 0 & 0 & A^j_{20} & 0 & 0 & 0\\
0 & 0 & 0 & 0 & 0 & 0 & 0 & P^j_1 & 0 & 0\\
0 & 0 & 0 & 0 & 0 & 0 & 0 & 0 & P^j_1 & 0\\
0 & 0 & 0 & 0 & 0 & 0 & 0 & 0 & 0 & P^j_1\\
-A^j_1 & -A^j_2 & -A^j_3 & -A^j_4 & -A^j_5 & -A^j_6 & 0 & -A^j_7 & -A^j_8 & -A^j_9\\
-A^j_{11} & -A^j_{12} & -A^j_{13} & -A^j_{14} & -A^j_{15} & 0 & -A^j_{16} & -A^j_{17} & -A^j_{18} & -A^j_{19}\\
-P^j_2 & -P^j_3 & -P^j_4 & -P^j_5 & -P^j_6 & -P^j_7 & -P^j_8 & -P^j_9 & -P^j_{10} & -P^j_{11}\\
-P^j_{12} & -P^j_{13} & -P^j_{14} & -P^j_{15} & -P^j_{16} & -P^j_{17} & -P^j_{18} & -P^j_{19} & -P^j_{20} & -P^j_{21}\\
-P^j_{22} & -P^j_{23} & -P^j_{24} & -P^j_{25} & -P^j_{26} & -P^j_{27} & -P^j_{28} & -P^j_{29} & -P^j_{30} & -P^j_{31}
\end{bmatrix}
\begin{Bmatrix}
U^j\\ V^j\\ W^j\\ \Phi^j\\ \Psi^j\\ U^j_{,z}\\ V^j_{,z}\\ W^j_{,z}\\ \Phi^j_{,z}\\ \Psi^j_{,z}
\end{Bmatrix}.
\tag{23}
$$

It is possible to write:

$$
\boldsymbol{D}^j\boldsymbol{X}^j_{,z}=\boldsymbol{A}^j\boldsymbol{X}^j\Rightarrow\boldsymbol{X}^j_{,z}=\boldsymbol{A}^{*j}\boldsymbol{X}^j.
\tag{24}
$$

Now, Eq. (24) can be solved considering the exponential matrix method:

$$
\boldsymbol{X}^j(h_j)=\boldsymbol{A}^{**j}\boldsymbol{X}^j(0)=\left[\sum_{i=0}^{M}\frac{(\boldsymbol{A}^{*j})^i}{i!}h^i_j\right]\boldsymbol{X}^j(0).
\tag{25}
$$

where $(\boldsymbol{A}^{*j})^0 = \boldsymbol{I}$ is the 10×10 identity matrix. The thickness of each j layer is h_j. Introducing local $\tilde{z}_j$ coordinate, its value is 0 at the bottom of the j layer and it is h_j at the top of the j layer.

The layerwise approach is achieved imposing congruence continuity conditions on displacements, electric potential, magnetic potential and equilibrium continuity conditions on transverse normal stresses, transverse shear stresses, transverse normal electric displacement and transverse normal magnetic induction. These conditions are imposed between the top (t) of the $j-1$ mathematical layer and the bottom (b) of the j mathematical layer. They can be written as:

$$u_b^j = u_t^{j-1}, \quad v_b^j = v_t^{j-1}, \quad w_b^j = w_t^{j-1}, \quad \phi_b^j = \phi_t^{j-1}, \quad \psi_b^j = \psi_t^{j-1} \tag{26a}$$

$$\sigma_{xz_b}^j = \sigma_{xz_t}^{j-1}, \quad \sigma_{yz_b}^j = \sigma_{yz_t}^{j-1}, \quad \sigma_{zz_b}^j = \sigma_{zz_t}^{j-1}, \quad \mathcal{D}_{z_b}^j = \mathcal{D}_{z_t}^{j-1}, \quad \mathcal{B}_{z_b}^j = \mathcal{B}_{z_t}^{j-1}. \tag{26b}$$

In a compact form, it is possible to write:

$$\begin{Bmatrix} U \\ V \\ W \\ \Phi \\ \Psi \\ U_{,z} \\ V_{,z} \\ W_{,z} \\ \Phi_{,z} \\ \Psi_{,z} \end{Bmatrix}_b^j = \begin{bmatrix} 1 & 0 & 0 & 0 & 0 & 0 & 0 & 0 & 0 & 0 \\ 0 & 1 & 0 & 0 & 0 & 0 & 0 & 0 & 0 & 0 \\ 0 & 0 & 1 & 0 & 0 & 0 & 0 & 0 & 0 & 0 \\ 0 & 0 & 0 & 1 & 0 & 0 & 0 & 0 & 0 & 0 \\ 0 & 0 & 0 & 0 & 1 & 0 & 0 & 0 & 0 & 0 \\ T_1 & 0 & T_2 & T_3 & T_4 & T_5 & 0 & 0 & 0 & 0 \\ 0 & T_6 & T_7 & T_8 & T_9 & 0 & T_{10} & 0 & 0 & 0 \\ T_{11} & T_{12} & T_{13} & 0 & 0 & 0 & 0 & T_{14} & T_{15} & T_{16} \\ T_{17} & T_{18} & T_{19} & 0 & 0 & 0 & 0 & T_{20} & T_{21} & T_{22} \\ T_{23} & T_{24} & T_{25} & 0 & 0 & 0 & 0 & T_{26} & T_{27} & T_{28} \end{bmatrix}^{j,j-1} \begin{Bmatrix} U \\ V \\ W \\ \Phi \\ \Psi \\ U_{,z} \\ V_{,z} \\ W_{,z} \\ \Phi_{,z} \\ \Psi_{,z} \end{Bmatrix}_t^{j-1} \Rightarrow \boldsymbol{X}_b^j = \boldsymbol{T}^{j,j-1} \boldsymbol{X}_t^{j-1} \tag{27}$$

where $\boldsymbol{T}^{j,j-1}$ is the transfer matrix that allows to implement the layerwise approach in the formulation.

In order to have the full solution along the thickness direction, the recursive substitution of Eq. (27) into Eq. (25) must be done. The resulting compact form is:

$$\boldsymbol{X}^M(h_M) = \boldsymbol{H}_m \boldsymbol{X}^1(0), \tag{28}$$

where matrix $\boldsymbol{H}_m = \boldsymbol{A}^{**M} \boldsymbol{T}^{M,M-1} \dots \boldsymbol{T}^{2,1} \boldsymbol{A}^{**1}$ is the multilayered matrix, including all peculiarities of the structure (material properties, in-plane dimensions, half-wave couple numbers, curvature terms, radii of curvature). $\boldsymbol{H}_m$ links the bottom ($\tilde{z}_1 = 0$) of the first (1) layer with the top ($\tilde{z}_M = h_M$) of the last (M) layer.

Constraint conditions are the simply-supported ones for all the four edges: harmonic forms naturally fulfill them. They can be explicitly written as:

$$\begin{aligned} &v^k = 0, \quad w^k = 0, \quad \phi^k = 0, \quad \psi^k = 0, \quad \sigma_{\alpha\alpha}^k = 0 \quad \text{for} \quad \alpha = 0, a, \\ &u^k = 0, \quad w^k = 0, \quad \phi^k = 0, \quad \psi^k = 0, \quad \sigma_{\beta\beta}^k = 0 \quad \text{for} \quad \beta = 0, b. \end{aligned} \tag{29}$$

Load boundary conditions can be imposed for sensor and actuator cases.

In the sensor case, where a transverse normal mechanical load is applied at the top of the shell, we have:

$$\sigma_{zz} = p_{z_t}, \quad \sigma_{\alpha z} = 0, \quad \sigma_{\beta z} = 0, \quad \phi = 0, \quad \psi = 0 \quad \text{for } z = +h/2. \tag{30a}$$

$$\sigma_{zz} = 0, \quad \sigma_{\alpha z} = 0, \quad \sigma_{\beta z} = 0, \quad \phi = 0, \quad \psi = 0 \quad \text{for } z = -h/2, \tag{30b}$$

In the actuator case, electric potentials and magnetic potentials can be applied at external surfaces:

$$\sigma_{zz} = 0, \quad \sigma_{\alpha z} = 0, \quad \sigma_{\beta z} = 0, \quad \phi = \phi_t, \quad \psi = \psi_t \quad \text{for } z = +h/2, \tag{31a}$$

$$\sigma_{zz} = 0, \quad \sigma_{\alpha z} = 0, \quad \sigma_{\beta z} = 0, \quad \phi = \phi_b, \quad \psi = \psi_b \quad \text{for } z = -h/2. \tag{31b}$$

Both sensor and actuator cases can be written in a general compact form as follows:

$$\begin{bmatrix} B_{1_t}^M & B_{2_t}^M & B_{3_t}^M & 0 & 0 & 0 & 0 & B_{4_t}^M & B_{5_t}^M & B_{6_t}^M \\ 0 & B_{7_t}^M & B_{8_t}^M & B_{9_t}^M & B_{10_t}^M & 0 & B_{11_t}^M & 0 & 0 & 0 \\ B_{12_t}^M & 0 & B_{13_t}^M & B_{14_t}^M & B_{15_t}^M & B_{16_t}^M & 0 & 0 & 0 & 0 \\ 0 & 0 & 0 & 1 & 0 & 0 & 0 & 0 & 0 & 0 \\ 0 & 0 & 0 & 0 & 1 & 0 & 0 & 0 & 0 & 0 \end{bmatrix} \begin{Bmatrix} U \\ V \\ W \\ \Phi \\ \Psi \\ U_{,z} \\ V_{,z} \\ W_{,z} \\ \Phi_{,z} \\ \Psi_{,z} \end{Bmatrix}_t^M = \begin{Bmatrix} P_z \\ 0 \\ 0 \\ \Phi \\ \Psi \end{Bmatrix}_t \Rightarrow \boldsymbol{B}_t^M \boldsymbol{X}^M(h_M) = \boldsymbol{P}_t, \tag{32}$$

$$\begin{bmatrix} B_{1_b}^1 & B_{2_b}^1 & B_{3_b}^1 & 0 & 0 & 0 & 0 & B_{4_b}^1 & B_{5_b}^1 & B_{6_b}^1 \\ 0 & B_{7_b}^1 & B_{8_b}^1 & B_{9_b}^1 & B_{10_b}^1 & 0 & B_{11_b}^1 & 0 & 0 & 0 \\ B_{12_b}^1 & 0 & B_{13_b}^1 & B_{14_b}^1 & B_{15_b}^1 & B_{16_b}^1 & 0 & 0 & 0 & 0 \\ 0 & 0 & 0 & 1 & 0 & 0 & 0 & 0 & 0 & 0 \\ 0 & 0 & 0 & 0 & 1 & 0 & 0 & 0 & 0 & 0 \end{bmatrix} \begin{Bmatrix} U \\ V \\ W \\ \Phi \\ \Psi \\ U_{,z} \\ V_{,z} \\ W_{,z} \\ \Phi_{,z} \\ \Psi_{,z} \end{Bmatrix}_b^1 = \begin{Bmatrix} P_z \\ 0 \\ 0 \\ \Phi \\ \Psi \end{Bmatrix}_b \Rightarrow \boldsymbol{B}_b^1 \boldsymbol{X}^1(0) = \boldsymbol{P}_b, \tag{33}$$

Eq. (28) allows Eq. (32) to be written as:

$$\boldsymbol{B}_t^M \boldsymbol{H}_m \boldsymbol{X}^1(0) = \boldsymbol{P}_t, \tag{34}$$

Eqs. (34) and (33) give the following algebraic system:

$$\begin{bmatrix} \boldsymbol{B}_t^M \boldsymbol{H}_m \\ \boldsymbol{B}_b^1 \end{bmatrix} \boldsymbol{X}^1(0) = \begin{Bmatrix} \boldsymbol{P}_t \\ \boldsymbol{P}_b \end{Bmatrix} \Rightarrow \boldsymbol{E} \boldsymbol{X}^1(0) = \boldsymbol{P}. \tag{35}$$

In the sensor configuration, the $\boldsymbol{P}$ vector has Φ_t, Ψ_t, Φ_b and Ψ_b equal zero; in the actuator configuration, the $\boldsymbol{P}$ vector has P_{z_t} and P_{z_b} equal zero.

Solving the linear system in Eq. (35), unknown vector $\boldsymbol{X}^1(0)$ at the bottom ($\tilde{z}_1 = 0$) of the first (1) mathematical layer is computed. In order to have the solution along the thickness direction, recursive substitution of Eq. (27) into Eq. (25) is mandatory. Thanks to the correct computation of the first derivatives in z of primary variables, stress, electric displacement and magnetic induction components can be exactly evaluated for each analyzed condition. The proposed mathematical formulation has been entirely implemented in an in-house academic Matlab (R2022a) code called *3DES* (*Three-Dimensional Exact Solutions*).

Table 1
Electro-magneto-elastic material characteristics for validation cases and new benchmarks.

	PZT-5	MSCP	$CoFe_2O_4$	$BaTiO_3$	Composite	Adaptive Wood
E_1 [GPa]	61.006	26.027	154.32	116.33	172.37	154.32
E_2 [GPa]	61.006	26.027	154.32	116.33	6.895	154.32
E_3 [GPa]	53.202	22.004	142.83	111.93	6.895	142.83
ν_{12}	0.34998	0.27585	0.36564	0.30709	0.25	0.36564
ν_{13}	0.37998	0.35392	0.40133	0.33362	0.25	0.40133
ν_{23}	0.37998	0.35392	0.40133	0.33362	0.25	0.40133
G_{12} [GPa]	22.59	10.2	56.5	44.5	3.447	56.5
G_{13} [GPa]	21.1	15.7	45.3	43	3.447	45.3
G_{23} [GPa]	21.1	15.7	45.3	43	1.379	45.3
e_{15} [C/m^2]	12.32	0	0	11.6	0	11.6
e_{24} [C/m^2]	12.32	0	0	11.6	0	11.6
e_{31} [C/m^2]	−7.2	0	0	−4.4	0	−4.4
e_{32} [C/m^2]	−7.2	0	0	−4.4	0	−4.4
e_{33} [C/m^2]	15.11	0	0	18.6	0	18.6
ϵ_1 [nF/m]	1.53	0.008854	0.08	11.2	0.008854	0.08
ϵ_2 [nF/m]	1.53	0.008854	0.08	11.2	0.008854	0.08
ϵ_3 [nF/m]	1.5	0.008854	0.093	12.6	0.008854	0.093
q_{15} [T]	0	21.6	550	0	0	560
q_{24} [T]	0	21.6	550	0	0	560
q_{31} [T]	0	−12.2	580.3	0	0	580
q_{32} [T]	0	−12.2	580.3	0	0	580
q_{33} [T]	0	31.3	699.7	0	0	700
μ_1 [nH/m]	$4\pi \cdot 10^2$	$5.4 \cdot 10^3$	$-590 \cdot 10^3$	$5 \cdot 10^3$	$4\pi \cdot 10^2$	$590 \cdot 10^3$
μ_2 [nH/m]	$4\pi \cdot 10^2$	$5.4 \cdot 10^3$	$-590 \cdot 10^3$	$5 \cdot 10^3$	$4\pi \cdot 10^2$	$590 \cdot 10^3$
μ_3 [nH/m]	$4\pi \cdot 10^2$	$5.4 \cdot 10^3$	$157 \cdot 10^3$	$10 \cdot 10^3$	$4\pi \cdot 10^2$	$157 \cdot 10^3$
d_1 [Ns/VC]	0	0	0	0	0	$3 \cdot 10^{-12}$
d_2 [Ns/VC]	0	0	0	0	0	$3 \cdot 10^{-12}$
d_3 [Ns/VC]	0	0	0	0	0	$3 \cdot 10^{-12}$

Table 2
First validation case: simply-supported multilayered (PZT-4/0°/90°/0°/PZT-4) spherical shell panel in sensor configuration. $P_{z_t} = 10\,000$ Pa, $P_{z_b} = 0$ Pa, $\Phi_t = \Phi_b = 0$ V. Imposed half-wave couples $m = n = 1$.

R_α/h	4	10	20	50	100
	u [10^{-6} m] ($\bar{z} = 0.75$ h)				
3D-u-ϕ [44]	2.2747	7.2142	18.227	51.566	106.04
3D-u-ϕ-ψ	2.2747	7.2142	18.227	51.566	106.04
	w [10^{-6} m] ($\bar{z} = 0.5$ h)				
3D-u-ϕ [44]	8.1441	29.243	69.761	185.52	372.91
3D-u-ϕ-ψ	8.1441	29.243	69.761	185.52	372.91
	$\sigma_{\alpha\alpha}$ [10^4 Pa] ($\bar{z} = 0.75$ h)				
3D-u-ϕ [44]	2.1226	10.213	20.405	42.092	75.084
3D-u-ϕ-ψ	2.1226	10.213	20.405	42.092	75.084
	σ_{zz} [10^3 Pa] ($\bar{z} = 0.95$ h)				
3D-u-ϕ [44]	8.4501	8.0275	8.2123	8.6185	8.8043
3D-u-ϕ-ψ	8.4501	8.0275	8.2123	8.6185	8.8043
	ϕ [V] ($\bar{z} = 0.15$ h)				
3D-u-ϕ [44]	73.405	61.114	18.425	−24.442	−40.096
3D-u-ϕ-ψ	73.405	61.114	18.425	−24.442	−40.096
	D_z [10^{-9} C/m^2] ($\bar{z} = 0.85$ h)				
3D-u-ϕ [44]	−0.90406	−2.9563	−7.4954	−20.662	−41.931
3D-u-ϕ-ψ	−0.90406	−2.9563	−7.4954	−20.662	−41.931

Table 3
First validation case: simply-supported multilayered (PZT-4/0°/90°/0°/PZT-4) spherical shell panel in actuator configuration. $\Phi_t = 100$ V, $\Phi_b = 0$ V, $P_{z_t} = P_{z_b} = 0$ Pa. Imposed half-wave couples $m = n = 1$.

R_α/h	4	10	20	50	100
	u [10^{-10} m] ($\bar{z} = 0.75$ h)				
3D-u-ϕ [44]	4.5586	6.4563	9.1110	11.592	12.591
3D-u-ϕ-ψ	4.5586	6.4563	9.1110	11.592	12.591
	w [10^{-10} m] ($\bar{z} = 0.5$ h)				
3D-u-ϕ [44]	6.1164	17.331	28.274	37.035	41.351
3D-u-ϕ-ψ	6.1164	17.331	28.274	37.035	41.351
	$\sigma_{\alpha\alpha}$ [Pa] ($\bar{z} = 0.75$ h)				
3D-u-ϕ [44]	−9.3659	−2.7655	1.2040	3.0518	4.8817
3D-u-ϕ-ψ	−9.3659	−2.7655	1.2040	3.0518	4.8817
	σ_{zz} [Pa] ($\bar{z} = 0.95$ h)				
3D-u-ϕ [44]	0.16537	−0.02447	−0.00976	0.01703	0.02348
3D-u-ϕ-ψ	0.16537	−0.02447	−0.00976	0.01703	0.02348
	ϕ [V] ($\bar{z} = 0.15$ h)				
3D-u-ϕ [44]	9.4888	10.841	11.050	11.108	11.117
3D-u-ϕ-ψ	9.4888	10.841	11.050	11.108	11.117
	D_z [10^{-9} C/m^2] ($\bar{z} = 0.85$ h)				
3D-u-ϕ [44]	−1.4074	−3.0520	−5.9535	−14.775	−29.519
3D-u-ϕ-ψ	−1.4074	−3.0520	−5.9535	−14.775	−29.519

3. Results

In this section, results coming from the formulation described in Section 2 are proposed. A first validation part is shown in order to compare the present exact 3D magneto-electro-elastic formulation (called 3D-u-ϕ-ψ) with a 3D magneto-elastic formulation (3D-u-ψ), a 3D electro-elastic formulation (3D-u-ϕ) and a 3D Semi-Analytical magneto-electro-elastic formulation (3D-SA). The acronym 3D-u-ϕ-ψ makes clear the main peculiarities of the present formulation: a three-dimensional exact model where primary variables are displacement components, electric and magnetic potentials (and related first derivatives in z). In the second part, new cases are proposed to understand the magneto-electro-elastic coupling effects for different geometries and different thickness ratios. Material layer effects, thickness layer effects and curvature effects are also investigated for both sensor and actuator configurations.

3.1. Validation cases

In this subsection, the validation of the present 3D-u-ϕ-ψ model is performed. Due to difficulties in finding 3D magneto-electro-elastic shell models for multilayered structures embedding both piezoelectric and piezomagnetic materials, three different 3D formulations have been used for the validation: a 3D analytical electro-elastic formulation [44], a 3D analytical magneto-elastic formulation [45] and a 3D

semi-analytical magneto-electro-elastic formulation [50]. In the present subsection, four different validation cases are proposed and they consider different geometries, materials and load boundary conditions in order to validate all the possible analyzable cases. As studied in Brischetto in [51,52], in order to have correct results for each thickness ratio, a number $M = 300$ of mathematical layers and an order for the exponential matrix $N = 3$ are satisfactory for each possible validation case.

In the first validation case, a simply-supported multilayered spherical shell panel is proposed. The layer stacking sequence is PZT-4/0°/90°/0°/PZT-4, from the bottom to the top. Each composite layer has thickness 0.3 h and each PZT-4 lamina has thickness 0.05 h. h is the total thickness of the structure. Multifield material are collected in Table 1 under PZT-4 and Composite columns. Geometrical data are: $a = b = \frac{\pi}{3} R_\alpha$, $R_\alpha = R_\beta = 10\,\text{m}$, h is variable and it depends on the thickness ratio R_α/h. Imposed half-wave couples (m, n) are $(1, 1)$. For the sensor configuration, $P_{z_t} = 10000\,\text{Pa}$ and $P_{z_b} = 0\,\text{Pa}$, $\Phi_t = \Phi_b = 0\,\text{V}$. For the actuator configuration, $\Phi_t = 100\,\text{V}$ and $\Phi_b = 0\,\text{V}$, $P_{z_t} = P_{z_b} = 0\,\text{Pa}$. The present case is proposed for both sensor and actuator configurations for different R_α/h thickness ratios. $R_\alpha/h = 4$ means thick spherical shell panel and $R_\alpha/h = 100$ means thin spherical shell panel. For the sensor (Table 2) and actuator (Table 3) configurations, 3D-u-ϕ-ψ model results have been compared with the reference electro-elastic results proposed in [44]. In Tables 2 and 3, six different variables (u, w, $\sigma_{\alpha\alpha}$, σ_{zz}, ϕ and D_z) are taken into account for comparisons with reference results at different thickness locations $\tilde{z}$. As can be clearly seen, a perfect match between results from 3D-u-ϕ-ψ model and reference results is achieved. This assessment permits to validate curvature effects, material layer effects, thickness layer effects and electro-elastic coupling for sensor and actuator configurations.

The second validation case is devoted to a simply-supported multilayered thin spherical shell. The layer stacking sequence is $CoFe_2O_4$/$BaTiO_3$ from the bottom to the top. Each layer is 0.5 h. Material properties of magnetostrictive $CoFe_2O_4$ and piezoelectric $BaTiO_3$ materials are collected in Table 1. Geometrical data for this validation case are: $a = b = 1\,\text{m}$, $R_\alpha = R_\beta = 10\,\text{m}$, $h = 0.1\,\text{m}$, half-wave couples $(m, n) = (1, 1)$. Two different configurations are validated: a sensor case where $P_{z_t} = 1\,\text{Pa}$ and $P_{z_b} = 0\,\text{Pa}$ are imposed with electric and magnetic potentials equal zero at the external surfaces; an electric actuator case where $\Phi_t = 1\,\text{V}$ and $\Phi_b = 0\,\text{V}$ without any applied mechanical loads and magnetic potentials ($\Psi_t = \Psi_b = 0\,\text{A}$). Results provided by the 3D-u-ϕ-ψ model are compared with results of the 3D Semi-Analytical (3D-SA) model in [50]. Tables 4 and 5 compare obtained scaled values ($\bar{u}$, $\bar{w}$, $\bar{\sigma}_{\alpha\alpha}$, $\bar{\sigma}_{\alpha z}$, $\bar{\sigma}_{zz}$, $\bar{\phi}$, $\bar{D}_z$, $\bar{\psi}$, $\bar{\mathcal{B}}_z$) with the reference results proposed in [50]. As can be seen in Tables 4 and 5, a very good match between the present 3D-u-ϕ-ψ model and the reference results is reached. The relative error is always less than 2%. This assessment has been used to validate the curvature terms, the material layer effects and the correct depiction of the magneto-electro-elastic coupling in a curved structure.

Validation case number three is a three-layered MSCP/PZT-5/MSCP simply-supported cylindrical shell panel. Material peculiarities in terms of elastic, piezoelectric, dielectric, piezomagnetic and magnetic permittivity coefficients are grouped in Table 1 under the proper columns. Each MSCP lamina has thickness value equals 0.02 m and PZT-5 core is 0.06 m. Geometrical data are: $a = \frac{\pi}{3} R_\alpha$, $b = 1\,\text{m}$, R_α is variable and depends on the R_α/h thickness ratio, $R_\beta = \infty$, $h = 0.1\,\text{m}$ (global thickness), half-wave couples (m, n) are $(1, 1)$. A sensor load boundary configuration is analyzed where $P_{z_t} = 1\,\text{Pa}$, $P_{z_b} = 0\,\text{Pa}$, $\Phi_t = \Phi_b = 0\,\text{V}$ and $\Psi_t = \Psi_b = 0\,\text{A}$. Results from 3D-$u$-$\phi$-$\psi$ model are compared with the ones presented in [50] using the 3D-SA formulation . For each proposed R_α, Table 6 shows a good match between 3D-u-ϕ-ψ results and reference results [50] in terms of primary variables (u and w) and secondary variables ($\sigma_{\alpha\alpha}$, $\sigma_{\alpha z}$ and $\sigma_{\beta z}$). The present assessment has been used to validate the curvature effect in only one direction, the material layer and thickness layer effects of multilayered curved smart structures.

Last validation case is about a simply-supported multilayered spherical shell panel with the following stacking sequence: $CoFe_2O_4$/0°/90°/0°/$CoFe_2O_4$ (from the bottom to the top). Each magnetostrictive $CoFe_2O_4$ lamina is 0.05 h and each Composite lamina is 0.3 h; h is the total thickness of the spherical shell panel. All material characteristics are exposed in Table 1. The spherical shell panel has the following

Table 4
Second validation case: simply-supported multilayered ($CoFe_2O_4$/$BaTiO_3$) spherical shell panel in sensor configuration. $P_{z_t} = 1\,\text{Pa}$, $P_{z_b} = 0\,\text{Pa}$, $\Phi_t = \Phi_b = 0\,\text{V}$, $\Psi_t = \Psi_b = 0\,\text{A}$. Imposed half-wave couples $m = n = 1$.

	$\tilde{z}$	3D-SA [50]	3D-u-ϕ-ψ
$\bar{u} = \frac{10^{10} u}{P_{z_t} h}$	h	−2.3538	−2.3540
$\bar{w} = \frac{10^{10} w}{P_{z_t} h}$	0.5 h	20.2981	20.3007
$\bar{\sigma}_{\alpha\alpha} = \frac{\sigma_{\alpha\alpha}}{P_{z_t}}$	h	23.3973	23.3990
$\bar{\sigma}_{\alpha z} = \frac{\sigma_{\alpha z}}{P_{z_t}}$	0.5 h	2.3310	2.3310
$\bar{\sigma}_{zz} = \frac{\sigma_{zz}}{P_{z_t}}$	h	1.0000	1.0000
$\bar{\phi} = \frac{10\phi}{h}$	0.5 h	0.4439	0.4437
$\bar{D}_z = 10^6 D_z$	0.5 h	8.4726	8.3698
$\bar{\psi} = \frac{\psi}{h} \cdot 10^{-3}$	0.5 h	−3.4800	−3.5026
$\bar{\mathcal{B}}_z = 10^6 \mathcal{B}_z$	0.5 h	0.6983	0.7063

Table 5
Second validation case: simply-supported multilayered ($CoFe_2O_4$/$BaTiO_3$) spherical shell panel in actuator configuration. $P_{z_t} = P_{z_b} = 0\,\text{Pa}$, $\Phi_t = 1\,\text{V}$, $\Phi_b = 0\,\text{V}$, $\Psi_t = \Psi_b = 0\,\text{A}$. Imposed half-wave couples $m = n = 1$.

	$\tilde{z}$	3D-SA [50]	3D-u-ϕ-ψ
$\bar{u} = \frac{10^5 u}{\Phi_t}$	h	1.6402	1.6056
$\bar{w} = \frac{10^6 w}{\Phi_t}$	0.5 h	−8.1141	−8.0063
$\bar{\sigma}_{\alpha\alpha} = \sigma_{\alpha\alpha} h \cdot 10^{-2}$	h	−3.2252	−3.1726
$\bar{\sigma}_{\alpha z} = \sigma_{\alpha z} h \cdot 10^{-3}$	0.5 h	5.2177	5.1717
$\bar{\sigma}_{zz} = \sigma_{zz} h \cdot 10^{-4}$	0.5 h	−3.9335	−3.9282
$\bar{\phi} = \frac{\phi}{\Phi_t}$	h	1.0000	1.0000
$\bar{D}_z = \frac{10^6 D_z h}{\Phi_t}$	0.5 h	−1.8452	−1.8361
$\bar{\psi} = \frac{\psi}{\Phi_t} \cdot 10^{-8}$	0.5 h	−4.5973	−4.6892
$\bar{\mathcal{B}}_z = 10^3 \mathcal{B}_z h$	0.5 h	9.2243	9.4558

Table 6
Third validation case: simply-supported multilayered ($MSCP$/PZT-5/$MSCP$) cylindrical shell panel in sensor configuration. $P_{z_t} = 1\,\text{Pa}$, $P_{z_b} = 0\,\text{Pa}$, $\Phi_t = \Phi_b = 0\,\text{V}$, $\Psi_t = \Psi_b = 0\,\text{A}$. Imposed half-wave couples $m = n = 1$.

R_α [m]	5	10	20	50	100
	$u\,[10^{-12}\,\text{m}]$ ($\tilde{z} = \text{h}$)				
3D-SA [50]	0.93	−14.21	−12.87	−6.47	−3.44
3D-u-ϕ-ψ	1.26	−14.75	−12.81	−6.45	−3.43
	$w\,[10^{-9}\,\text{m}]$ ($\tilde{z} = \text{h}$)				
3D-SA [50]	1.55	2.12	2.35	2.42	2.43
3D-u-ϕ-ψ	1.55	2.12	2.35	2.42	2.43
	$\sigma_{\alpha\alpha}$ [Pa] ($\tilde{z} = \text{h}$)				
3D-SA [50]	13.75	13.71	12.30	10.92	10.39
3D-u-ϕ-ψ	13.83	13.81	12.41	11.03	10.50
	$\sigma_{\alpha z}$ [Pa] ($\tilde{z} = 0.8$ h)				
3D-SA [50]	0.18	0.13	0.08	0.03	0.02
3D-u-ϕ-ψ	0.18	0.13	0.08	0.03	0.02
	$\sigma_{\beta z}$ [Pa] ($\tilde{z} = 0.8$ h)				
3D-SA [50]	0.97	1.39	1.60	1.69	1.71
3D-u-ϕ-ψ	0.97	1.40	1.60	1.69	1.71

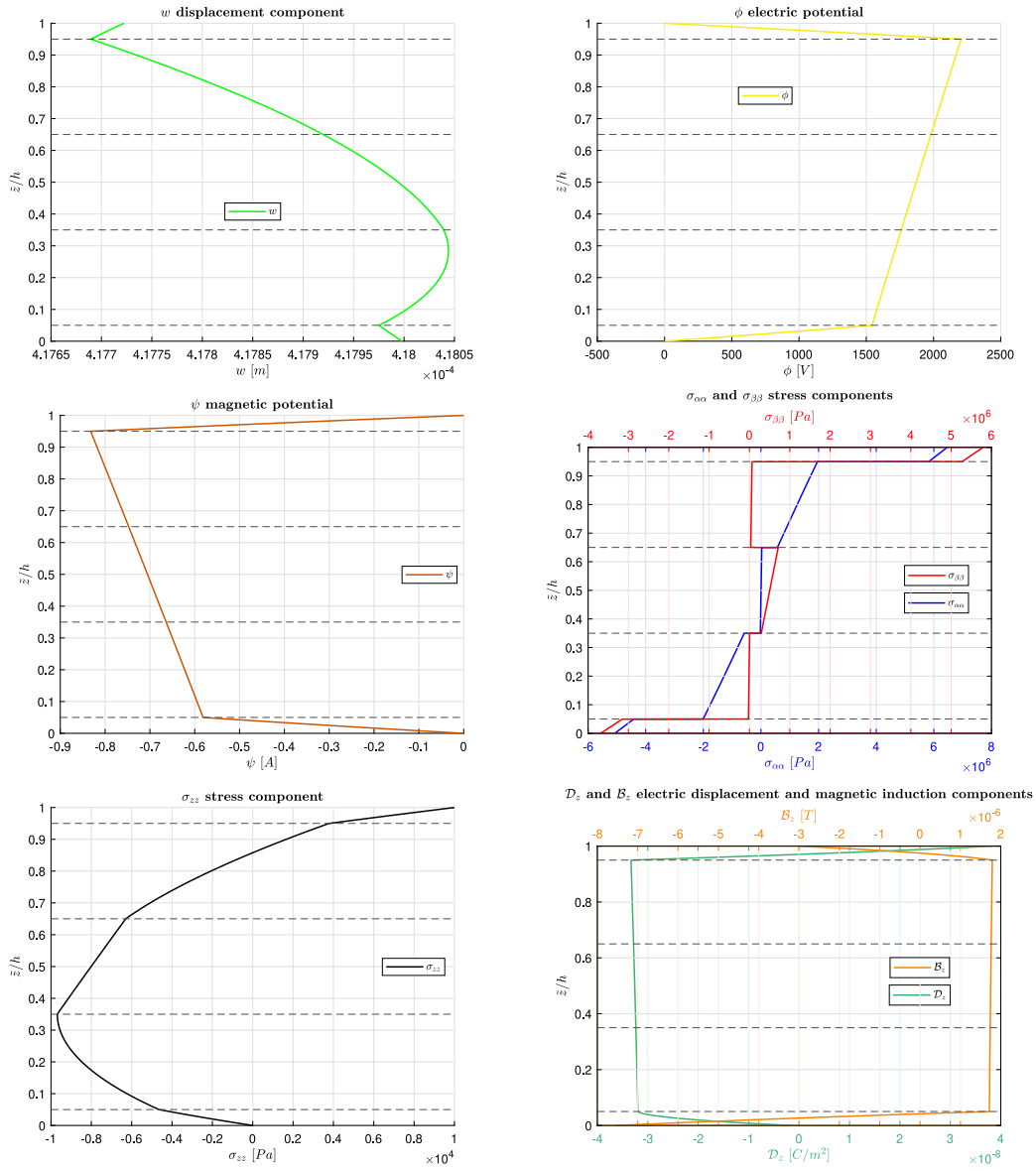

Fig. 4. Second new case in sensor configuration. Simply-supported multilayered (Adaptive Wood/0°/90°/0°/Adaptive Wood) cylindrical shell panel for $R_\alpha/h = 50$. $P_{z_t} = 10000\,\text{Pa}$, $P_{z_b} = 0\,\text{Pa}$, $\Phi_t = \Phi_b = 0\,\text{V}$, $\Psi_t = \Psi_b = 0\,\text{A}$. Imposed half-wave couples $m = 2$ and $n = 1$.

dimensions: $a = b = \frac{\pi}{3}R_\alpha$, $R_\alpha = R_\beta = 10\,\text{m}$; thickness h and R_α/h thickness ratios are variable. Half-wave couples (m, n) are $(1, 1)$. Both sensor and actuator load boundary conditions are analyzed. In the sensor configuration, load boundary conditions are: $P_{z_t} = 10000\,\text{Pa}$ and $P_{z_b} = 0\,\text{Pa}$, and magnetic potential equals zero at the outer surfaces. In the actuator configuration, load boundary conditions are: $\Psi_t = 10\,\text{A}$ and $\Psi_b = 0\,\text{A}$ without any mechanical loads applied at the outer surfaces. Reference results for this assessment are from the work by Brischetto and Cesare for multilayered magneto-elastic shells [45]. In Tables 7 and 8, displacements υ and w, stresses $\sigma_{\alpha\beta}$ and σ_{zz}, magnetic potential ψ and magnetic induction component $\mathcal{B}_z$ are compared with the reference results [45]. Results show a perfect accordance for each variable in any thickness ratio case. In this way, the capacity to evaluate curvature effects, material layer effects, thickness layer effects and the magneto-elastic couplings is validated.

From this brief validation case description, all the possible effect investigations for multilayered curved structures embedding piezoelectric and/or piezomagnetic laminae (curvature effects, material layer effects, thickness layer effects and magneto-electro-elastic couplings) are validated considering a number of mathematical layers $M = 300$ and an order of the exponential matrix $N = 3$.

3.2. New cases

In this subsection, three new cases are proposed involving simply-supported multilayered cylinders, cylindrical shell panels and spherical shells. The following benchmark cases are given considering thick, moderately thick, moderately thin and thin structures in terms of R_α/h. Tabular values at specific $\bar{z}$ positions and graphical trends along the thickness direction displaying eight different variables (w, ϕ, ψ, $\sigma_{\alpha\alpha}$, $\sigma_{\beta\beta}$, σ_{zz}, D_z and $\mathcal{B}_z$) are proposed. As stated in the validation cases subsection, these new cases are investigated considering in the model $M = 300$ mathematical layers and $N = 3$ as order of the exponential matrix. All three cases consider a stacking sequence, from the bottom to the top, Adaptive Wood/0°/90°/0°/Adaptive Wood. A single adaptive wood external layer has 0.05 h thickness and a single composite layer has 0.3 h thickness. h is the total thickness of the structure. Elastic, piezoelectric and piezomagnetic characteristics of materials are collected in Table 1. For each case, both sensor and actuator configurations

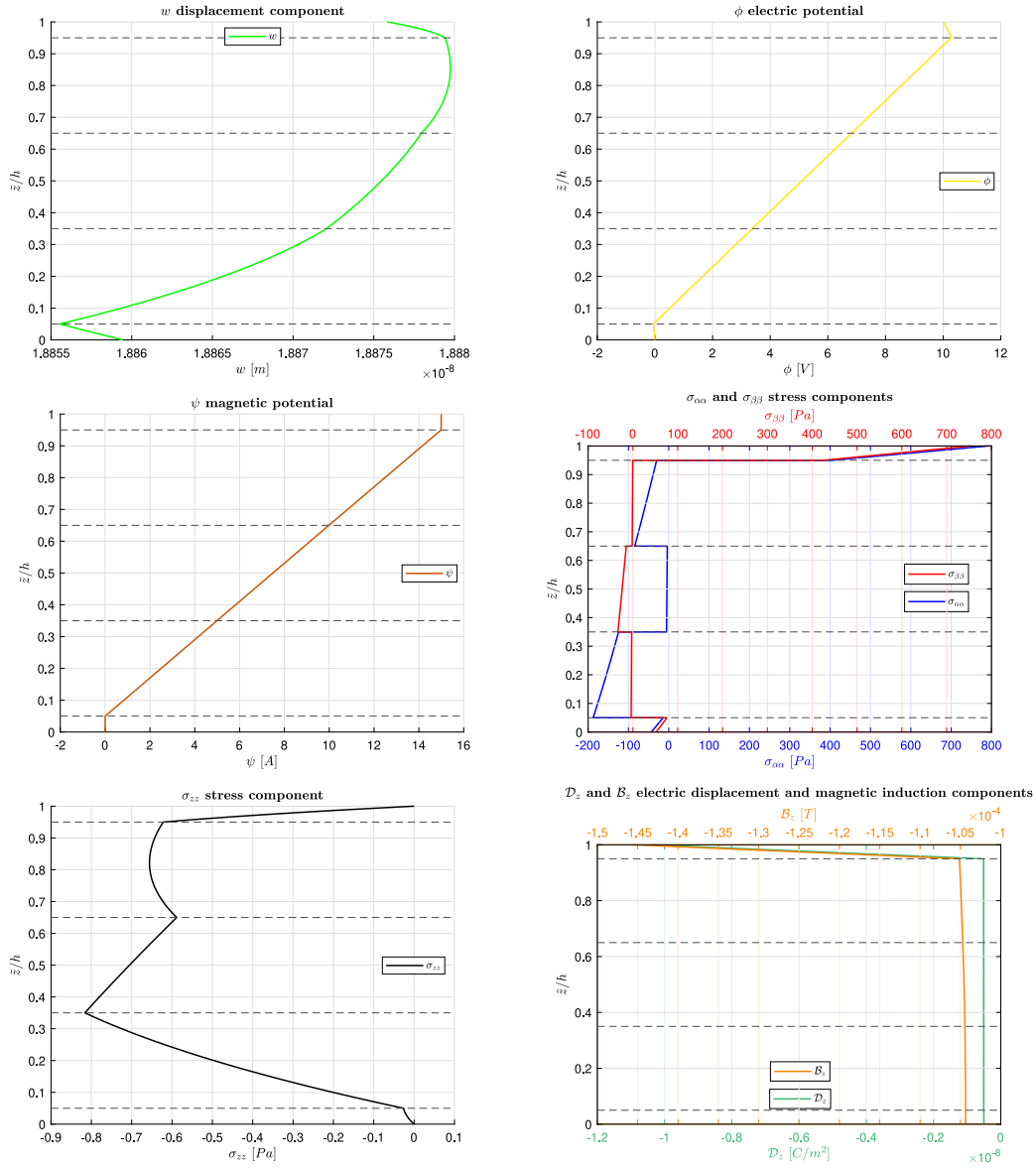

Fig. 5. Second new case in actuator configuration. Simply-supported multilayered (Adaptive Wood/0°/90°/0°/Adaptive Wood) cylindrical shell panel for $R_\alpha/h = 50$. $\Phi_t = 10\,\text{V}$, $\Phi_b = 0\,\text{V}$, $\Psi_t = 15\,\text{A}$, $\Psi_b = 0\,\text{A}$, $P_{z_t} = P_{z_b} = 0\,\text{Pa}$. Imposed half-wave couples $m = 2$ and $n = 1$.

are analyzed. The imposed sensor load boundary conditions are: $P_{z_t} = 10000\,\text{Pa}$, $P_{z_b} = 0\,\text{Pa}$, $\Phi_t = \Phi_b = 0\,\text{V}$, $\Psi_t = \Psi_b = 0\,\text{A}$. The imposed actuator load boundary conditions are: $\Phi_t = 10\,\text{V}$, $\Phi_b = 0\,\text{V}$, $\Psi_t = 15\,\text{A}$, $\Psi_b = 0\,\text{A}$, $P_{z_t} = 0 = P_{z_b} = 0\,\text{Pa}$.

The first new case regards a simply-supported multilayered cylinder. Geometrical data are: $a = 2\pi R_\alpha$, b = 10 m, $R_\alpha = 10\,\text{m}$, $R_\beta = \infty$, h is variable as R_α/h thickness ratio. Half-wave couples (m, n) are $(2, 1)$. In Tables 9 and 10, w, ϕ, ψ, $\sigma_{\alpha\alpha}$, $\sigma_{\beta\beta}$, σ_{zz}, $\mathcal{D}_z$ and $\mathcal{B}_z$ at specific $\tilde{z}$ coordinates are proposed for sensor and actuator configurations, respectively. It is possible to notice the increase in absolute value of w displacement for sensor configuration as the thickness ratio increases, this is due to the smaller stiffness of the structure. The same consideration is valid for stresses $\sigma_{\alpha\alpha}$, electric displacement $\mathcal{D}_z$ and magnetic induction $\mathcal{B}_z$. For the actuator configuration, the application of electric and magnetic potentials at the outer surfaces gives a different deformation behavior in relation to the thickness of the structure. In Figs. 2 and 3, the eight aforementioned variables are reported for $R_\alpha/h = 20$ thickness ratio for sensor and actuator load boundary conditions, respectively. The horizontal black dot lines indicates the interfaces between two physical layers. For each proposed variable, the change in slope in correspondence of each physical layer is clear thanks the correct depiction of the zig-zag effect. In addition, the layerwise approach is correctly implemented in the model; in fact, primary variables (w, ϕ and ψ), transverse normal stress (σ_{zz}), transverse normal electric displacement ($\mathcal{D}_z$) and transverse normal magnetic induction ($\mathcal{B}_z$) are continuous along the thickness direction for equilibrium or congruence reasons. In-plane normal stresses $\sigma_{\alpha\alpha}$ and $\sigma_{\beta\beta}$ show the typical non-continuous trend along the thickness direction because equilibrium condition impositions are not necessary at each interface for these variables. Load boundary conditions are correctly imposed for both sensor and actuator configurations: it is clearly visible in values ϕ, ψ and σ_{zz} at external surfaces. In the sensor case, electric and magnetic potentials are set to zero on the outer surfaces; the transverse normal mechanical load is applied in terms of the transverse normal stress σ_{zz} on the outer surfaces, and these values are 10000 Pa and 0 Pa at the top and bottom, respectively. In the actuator case, the transverse normal

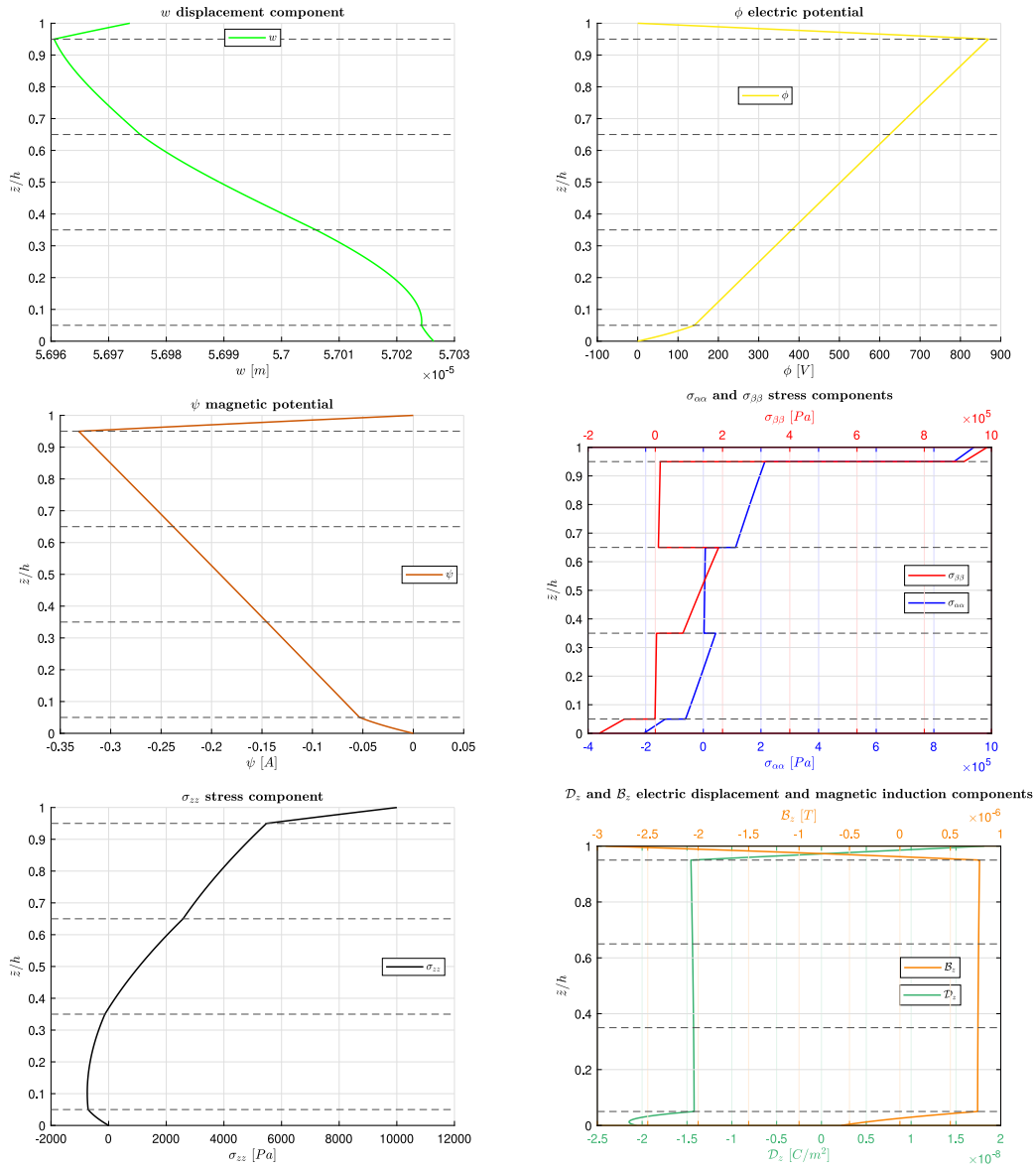

Fig. 6. Third new case in sensor configuration. Simply-supported multilayered (Adaptive Wood/0°/90°/0°/Adaptive Wood) spherical shell panel for $R_\alpha/h = 20$. $P_{z_t} = 10000\,\text{Pa}$, $P_{z_b} = 0\,\text{Pa}$, $\Phi_t = \Phi_b = 0\,\text{V}$, $\Psi_t = \Psi_b = 0\,\text{A}$. Imposed half-wave couples $m = n = 1$.

stress σ_{zz} on the outer surfaces is zero. The electric potential is set to 10 V at the top and 0 V at the bottom. The magnetic potential is set to 15 A at the top and 0 A at the bottom.

In the second case, a simply-supported multilayered cylindrical shell panel is proposed. Geometrical data are the following: $a = \frac{\pi}{3}R_\alpha$, b $= 10\,\text{m}$, $R_\alpha = 10\,\text{m}$, $R_\beta = \infty$, h is variable as the R_α/h thickness ratio. Half-wave couples (m, n) are $(2, 1)$. In Tables 11 and 12, the same eight variables taken into account for the first case are here proposed. Also for this case, in sensor configuration the increasing of primary variables (w, ϕ, ψ) and secondary variables (σ_{zz}, D_z and $\mathcal{B}_z$) is obtained for thinner structures due to their smaller stiffness. In the actuator configuration, trends for primary and secondary variables have some smaller differences between them when the thickness changes. In Figs. 4 and 5, the same eight variables are proposed in a graphical form for $R_\alpha/h = 50$ in both sensor and actuator configurations. It is possible to notice the zig-zag effect due to the change in slope at each k layer having different physical properties (expressed with the dotted horizontal black lines) and the correct imposition of the layerwise approach for w, ϕ, ψ, σ_{zz}, D_z and $\mathcal{B}_z$ variables via the opportune considerations for equilibrium and congruence physical conditions. Load boundary conditions are correctly imposed: $P_{z_t} = 10000\,\text{Pa}$, $P_{z_b} = 0\,\text{Pa}$, $\Phi_t = \Phi_b = 0\,\text{V}$, $\Psi_t = \Psi_b = 0\,\text{A}$ at external surfaces for the sensor case (Fig. 4); $\Phi_t = 10\,\text{V}$, $\Phi_b = 0\,\text{V}$, $\Psi_t = 15\,\text{A}$, $\Psi_b = 0\,\text{A}$, $P_{z_t} = 0 = P_{z_b} = 0\,\text{Pa}$ at external surfaces for the actuator case (Fig. 5).

The last case involves a simply-supported multilayered spherical shell. Geometrical data are: $a = \frac{\pi}{3}R_\alpha$, b $= \frac{\pi}{3}R_\beta$, $R_\alpha = R_\beta = 10\,\text{m}$. h is variable as the R_α/h thickness ratio. Half-wave couples (m, n) are $(1, 1)$. In Tables 13 and 14, w, ϕ, ψ, $\sigma_{\alpha\alpha}$, $\sigma_{\beta\beta}$, σ_{zz}, D_z and $\mathcal{B}_z$ variables are proposed for different $\bar{z}$ and R_α/h for both load boundary configurations. In the sensor configuration, w displacement increases for bigger R_α/h values. As curvature and thickness layer effects are relevant for thick and moderately thick structures, the increasing behavior seen for the displacement w is not also clear for the electric and magnetic potentials (ϕ and ψ). Electric displacement (D_z) and magnetic induction ($\mathcal{B}_z$) follows the w displacement trend, they increase in absolute value for thinner geometries. In the actuator case, ϕ does not have an increasing trend for thinner structures, meanwhile, w and ψ slightly increases for thinner spherical shells. The same increasing trend of ψ is valid in

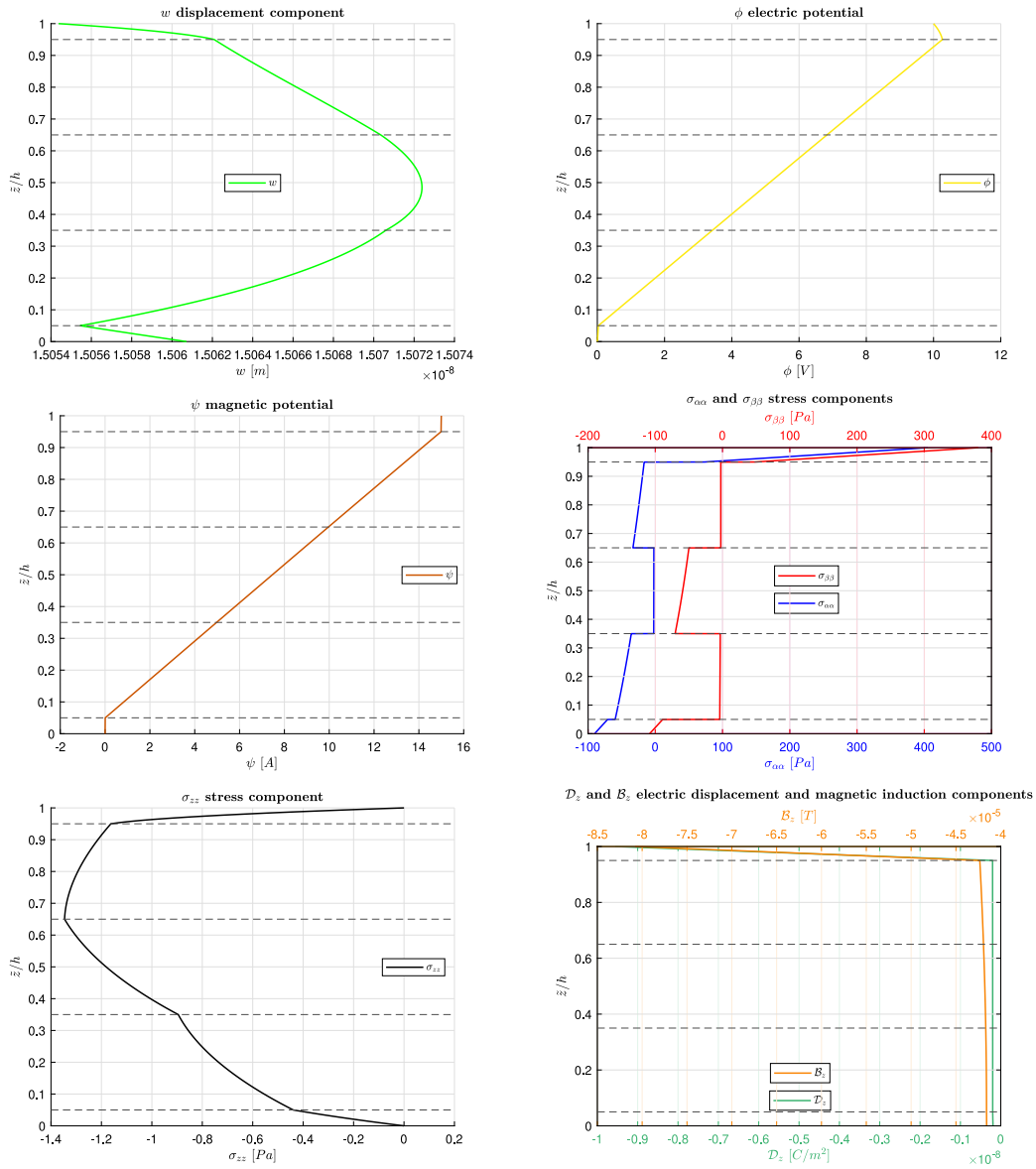

Fig. 7. Third new case in actuator configuration. Simply-supported multilayered (Adaptive Wood/0°/90°/0°/Adaptive Wood) spherical shell panel for $R_\alpha/h = 20$. $\Phi_t = 10\,\mathrm{V}$, $\Phi_b = 0\,\mathrm{V}$, $\Psi_t = 15\,\mathrm{A}$, $\Psi_b = 0\,\mathrm{A}$, $P_{z_t} = P_{z_b} = 0\,\mathrm{Pa}$. Imposed half-wave couples $m = n = 1$.

terms of absolute value for the electric displacement and the magnetic induction. Figs. 6 and 7 show the behavior along the thickness direction, for $R_\alpha/h = 20$, of the same eight variables proposed in tabular form for both load boundary conditions. The zig-zag effect is clear for both sensor and actuator configurations as the change in slope occurs for each layer of the structure having different physical properties. Layerwise approach is clear for both load boundary configurations. In particular, discontinuities in correspondence of physical layers for $\sigma_{\alpha\alpha}$ and $\sigma_{\beta\beta}$ are evident because interlaminar continuity conditions have not been enforced in these cases. Displacement w, electric potential ϕ, magnetic potential ψ, transverse normal stress σ_{zz}, transverse normal electric displacement D_z and transverse normal magnetic induction B_z are continuous along the thickness direction for equilibrium or congruence reasons. Furthermore, load boundary conditions are correctly imposed for both sensor and actuator configurations as can be seen by the values reached at the outer surfaces for σ_{zz}, ϕ and ψ trends. In the sensor case, electric and magnetic potentials are set to zero at external surfaces; the transverse normal mechanical load is applied in terms of the transverse normal stress σ_{zz} at external surfaces, and these values are 10000 Pa and 0 Pa at the top and bottom, respectively. In the actuator case, the transverse normal stress σ_{zz} at external surfaces is zero. The electric potential is 10 V at the top and 0 V at the bottom. The magnetic potential is 15 A at the top and 0 A at the bottom.

By carefully observing the three proposed cases, it can be noted that the cylinder presents a greater rigidity than the cylindrical panel due to its closed, circular and symmetric structure. In the case of spherical shells, the presence of two radii of curvature significantly complicates the behavior of the multifield variables along the thickness direction due to the presence of couplings between in-plane and out-of-plane variables.

4. Conclusions

The present work is devoted to the investigation of simply-supported multilayered smart shell structures embedding piezomagnetic and piezoelectric layers. Thanks to the mixed curvilinear orthogonal reference system and a three-dimensional approach, several multilayered

Table 7
Fourth validation case: simply-supported multilayered ($CoFe_2O_4$/0°/90°/0°/$CoFe_2O_4$) spherical shell panel in sensor configuration. $P_{z_t} = 10\,000$ Pa, $P_{z_b} = 0$ Pa, $\Psi_t = \Psi_b = 0$ A. Imposed half-wave couples $m = n = 1$.

R_α/h	4	10	20	50	100
	v [10^{-5} m] ($\bar{z} = 0$)				
3D-u-ψ [45]	0.3044	0.9694	2.0531	4.9566	9.5538
3D-u-ϕ-ψ	0.3044	0.9694	2.0531	4.9566	9.5538
	w [10^{-5} m] ($\bar{z} = h$)				
3D-u-ψ [45]	1.0395	2.7460	6.2414	16.702	33.673
3D-u-ϕ-ψ	1.0395	2.7460	6.2414	16.702	33.673
	$\sigma_{\alpha\beta}$ [10^4 Pa] ($\bar{z} = 0.75$ h)				
3D-u-ψ [45]	0.5305	1.3825	3.2764	9.3166	19.255
3D-u-ϕ-ψ	0.5305	1.3825	3.2764	9.3166	19.255
	σ_{zz} [10^3 Pa] ($\bar{z} = 0.50$ h)				
3D-u-ψ [45]	4.0292	2.1904	2.3206	3.6204	4.2857
3D-u-ϕ-ψ	4.0292	2.1904	2.3206	3.6204	4.2857
	ψ [A] ($\bar{z} = 0.75$ h)				
3D-u-ψ [45]	−0.0822	−0.0818	−0.0693	−0.0464	−0.0356
3D-u-ϕ-ψ	−0.0822	−0.0818	−0.0693	−0.0464	−0.0356
	$\mathcal{B}_z$ [10^{-7} T] ($\bar{z} = 0.50$ h)				
3D-u-ψ [45]	0.5704	1.1208	2.3452	6.1057	12.221
3D-u-ϕ-ψ	0.5704	1.1208	2.3452	6.1057	12.221

Table 8
Fourth validation case: simply-supported multilayered ($CoFe_2O_4$/0°/90°/0°/$CoFe_2O_4$) spherical shell panel in actuator configuration. $P_{z_t} = P_{z_b} = 0$ Pa, $\Psi_t = 10$ A, $\Psi_b = 0$ A. Imposed half-wave couples $m = n = 1$.

R_α/h	4	10	20	50	100
	v [10^{-9} m] ($\bar{z} = 0$)				
3D-u-ψ [45]	1.8657	3.5065	4.6059	5.2052	5.3381
3D-u-ϕ-ψ	1.8657	3.5065	4.6059	5.2052	5.3381
	w [10^{-8} m] ($\bar{z} = h$)				
3D-u-ψ [45]	0.6067	0.8023	1.1006	1.3465	1.3751
3D-u-ϕ-ψ	0.6067	0.8023	1.1006	1.3465	1.3751
	$\sigma_{\alpha\beta}$ [Pa] ($\bar{z} = 0.75$ h)				
3D-u-ψ [45]	6.2314	6.5530	7.8759	9.5701	10.224
3D-u-ϕ-ψ	6.2314	6.5530	7.8759	9.5701	10.224
	σ_{zz} [Pa] ($\bar{z} = 0.50$ h)				
3D-u-ψ [45]	1.5245	−0.4844	−0.4839	−0.1347	−0.0380
3D-u-ϕ-ψ	1.5245	−0.4844	−0.4839	−0.1347	−0.0380
	ψ [A] ($\bar{z} = 0.75$ h)				
3D-u-ψ [45]	7.4013	7.7094	7.7585	7.7726	7.7747
3D-u-ϕ-ψ	7.4013	7.7094	7.7585	7.7726	7.7747
	$\mathcal{B}_z$ [10^{-5} T] ($\bar{z} = 0.50$ h)				
3D-u-ψ [45]	−0.5437	−1.3884	−2.7866	−6.9737	−13.950
3D-u-ϕ-ψ	−0.5437	−1.3884	−2.7866	−6.9737	−13.950

Table 9
First new case in sensor configuration. Simply-supported multilayered (Adaptive Wood/0°/90°/0°/Adaptive Wood) cylinder. $P_{z_t} = 10\,000$ Pa, $P_{z_b} = 0$ Pa, $\Phi_t = \Phi_b = 0$ V, $\Psi_t = \Psi_b = 0$ A. Imposed half-wave couples $m = 2$ and $n = 1$.

R_α/h	4	10	20	50	100
	w [10^{-6} m] ($\bar{z} = 0.5$ h)				
	6.5344	17.508	36.782	93.568	187.23
	ϕ [10^2 V] ($\bar{z} = 0.75$ h)				
	3.6461	4.7409	4.1151	3.0093	2.5361
	ψ [10^{-2} A] ($\bar{z} = 0.25$ h)				
	−4.4639	−5.4050	−1.2219	3.7816	5.7201
	$\sigma_{\alpha\alpha}$ [10^5 Pa] ($\bar{z} = h$)				
	1.3839	3.6260	6.7083	14.298	26.405
	$\sigma_{\beta\beta}$ [10^4 Pa] ($\bar{z} = 0$)				
	−4.3302	−9.5112	−2.3032	39.514	113.30
	σ_{zz} [10^3 Pa] ($\bar{z} = 0.5$ h)				
	4.5111	4.4206	4.5593	4.7995	4.8989
	$\mathcal{D}_z$ [10^{-9} C/m^2] ($\bar{z} = 0.5$ h)				
	−1.8179	−5.9474	−13.523	−35.636	−71.913
	$\mathcal{B}_z$ [10^{-7} T] ($\bar{z} = 0.5$ h)				
	1.1003	3.3073	7.3585	19.179	38.565

Table 10
First new case in actuator configuration. Simply-supported multilayered (Adaptive Wood/0°/90°/0°/Adaptive Wood) cylinder. $\Phi_t = 10$ V, $\Phi_b = 0$ V, $\Psi_t = 15$ A, $\Psi_b = 0$ A, $P_{z_t} = P_{z_b} = 0$ Pa. Imposed half-wave couples $m = 2$ and $n = 1$.

R_α/h	4	10	20	50	100
	w [10^{-10} m] ($\bar{z} = 0.5$ h)				
	15.064	28.075	31.171	18.598	−8.9535
	ϕ [V] ($\bar{z} = 0.75$ h)				
	7.9685	8.0075	7.9212	7.8728	7.8642
	ψ [A] ($\bar{z} = 0.25$ h)				
	3.0534	3.2892	3.3250	3.3351	3.3365
	$\sigma_{\alpha\alpha}$ [10^2 Pa] ($\bar{z} = h$)				
	5.4070	3.2691	2.6784	3.3545	5.6433
	$\sigma_{\beta\beta}$ [Pa] ($\bar{z} = 0$)				
	−6.9878	−6.3866	59.383	238.39	495.29
	σ_{zz} [10^{-2} Pa] ($\bar{z} = 0.5$ h)				
	−27.523	−36.647	−17.036	−4.098	−1.3964
	$\mathcal{D}_z$ [10^{-11} C/m^2] ($\bar{z} = 0.5$ h)				
	−4.1020	−10.220	−20.346	−50.732	−101.39
	$\mathcal{B}_z$ [10^{-6} T] ($\bar{z} = 0.5$ h)				
	−8.1589	−20.839	−41.807	−104.61	−209.25

curved structures can be investigated in sensor and actuator configurations via a unique and general formulation. A set of five three-dimensional second-order differential equations is proposed for the coupling between magnetic, electric and elastic fields. The solution methodology involves Navier harmonic forms and the use of the exponential matrix method. The proposed validation cases have been used to assess the present 3D magneto-electro-elastic formulation for thick and thin curved structures in both sensor and actuator configurations in terms of displacements, stresses, magnetic and electric potentials, electric displacement and magnetic induction components. From these validation cases, it is clear the correct depiction of all effects for each thickness ratio. In the new cases, three different simply-supported shell structures (cylinders, cylindrical panels and spherical panels) have been proposed. Load boundary conditions were correctly imposed in both sensor and actuator configurations. Congruence and equilibrium conditions between two adjacent layers consent to have a layerwise model. Zig-zag effects, magneto-electro-elastic couplings, curvature effects, thickness and material layer effects are clearly visible in trends along the thickness direction for displacements, electric and magnetic potentials, electric displacement, magnetic induction and stresses. The present 3D formulation coupling magnetic, electric and elastic fields permits to have a novel and unified model for static analysis of several curved multilayered smart structures. The use of the mixed curvilinear reference system is able to model cylinders, cylindrical panels and spherical shells only by considering proper radii of curvature in the two in-plane directions. In literature, the other 3D magneto-electro-elastic formulations cannot consider different curved structures with a unique set of equations in layerwise form. New proposed cases are useful to those scientists involved in the developing of 2D numerical or analytical theories for smart structures to better understand the static behavior of shells in sensor and actuator configurations. Future developments of the

Table 11
Second new case in sensor configuration. Simply-supported multilayered (Adaptive Wood/0°/90°/0°/Adaptive Wood) cylindrical shell panel. P_{z_t} = 10 000 Pa, P_{z_b} = 0 Pa, $\Phi_t = \Phi_b = 0$ V, $\Psi_t = \Psi_b = 0$ A. Imposed half-wave couples $m = 2$ and $n = 1$.

R_α/h	4	10	20	50	100
	w [10^{-6} m] ($\bar{z} = 0.5$ h)				
	4.4511	15.211	50.750	417.99	2164.6
	ϕ [10^{2} V] ($\bar{z} = 0.75$ h)				
	2.6633	5.5804	9.6049	20.552	31.454
	ψ [10^{-2} A] ($\bar{z} = 0.25$ h)				
	−8.7907	−19.627	−32.762	−63.618	−81.553
	$\sigma_{\alpha\alpha}$ [10^{5} Pa] ($\bar{z} =$ h)				
	1.3464	3.9753	12.296	64.637	200.73
	$\sigma_{\beta\beta}$ [10^{4} Pa] ($\bar{z} = 0$)				
	−7.9423	−28.775	−85.622	−368.66	−777.56
	σ_{zz} [10^{2} Pa] ($\bar{z} = 0.5$ h)				
	48.834	29.359	−3.5812	−80.084	−139.78
	D_z [10^{-10} C/m^2] ($\bar{z} = 0.5$ h)				
	−2.6586	−7.3118	−33.117	−325.83	−1738.7
	$\mathcal{B}_z$ [10^{-8} T] ($\bar{z} = 0.5$ h)				
	2.6449	5.1440	18.846	175.01	929.76

Table 12
Second new case in actuator configuration. Simply-supported multilayered (Adaptive Wood/0°/90°/0°/Adaptive Wood) cylindrical shell panel. $\Phi_t = 10$ V, $\Phi_b = 0$ V, $\Psi_t = 15$ A, $\Psi_b = 0$ A, $P_{z_t} = P_{z_b} = 0$ Pa. Imposed half-wave couples $m = 2$ and $n = 1$.

R_α/h	4	10	20	50	100
	w [10^{-9} m] ($\bar{z} = 0.5$ h)				
	−3.9449	−1.502	1.4322	18.875	60.463
	ϕ [V] ($\bar{z} = 0.75$ h)				
	7.4890	7.9237	7.9480	7.9715	7.9572
	ψ [A] ($\bar{z} = 0.25$ h)				
	2.3452	3.1423	3.2867	3.3288	3.3350
	$\sigma_{\alpha\alpha}$ [10^{2} Pa] ($\bar{z} =$ h)				
	21.263	10.884	7.1482	7.9119	12.144
	$\sigma_{\beta\beta}$ [10^{1} Pa] ($\bar{z} = 0$)				
	7.7801	4.6110	2.9391	5.1933	29.681
	σ_{zz} [10^{-1} Pa] ($\bar{z} = 0.5$ h)				
	−40.831	−1.9185	−3.3529	−7.0557	−5.8141
	D_z [10^{-11} C/m^2] ($\bar{z} = 0.5$ h)				
	−4.1107	−10.284	−20.337	−50.820	−101.91
	$\mathcal{B}_z$ [10^{-6} T] ($\bar{z} = 0.5$ h)				
	−7.6307	−20.585	−41.673	−104.55	−209.22

Table 13
Third new case in sensor configuration. Simply-supported multilayered (Adaptive Wood/0°/90°/0°/Adaptive Wood) spherical shell panel. P_{z_t} = 10 000 Pa, P_{z_b} = 0 Pa, $\Phi_t = \Phi_b = 0$ V, $\Psi_t = \Psi_b = 0$ A. Imposed half-wave couples $m = n = 1$.

R_α/h	4	10	20	50	100
	w [10^{-6} m] ($\bar{z} = 0.5$ h)				
	8.7831	24.339	56.989	158.29	321.88
	ϕ [10^{2} V] ($\bar{z} = 0.75$ h)				
	5.1048	7.0348	7.0580	5.0304	3.7952
	ψ [10^{-2} A] ($\bar{z} = 0.25$ h)				
	−6.7761	−13.985	−11.453	−1.5543	3.5516
	$\sigma_{\alpha\alpha}$ [10^{5} Pa] ($\bar{z} =$ h)				
	1.7390	4.7094	9.3876	18.123	29.484
	$\sigma_{\beta\beta}$ [10^{4} Pa] ($\bar{z} = 0$)				
	−3.3778	−14.893	−16.653	39.874	157.78
	σ_{zz} [10^{3} Pa] ($\bar{z} = 0.5$ h)				
	3.5578	1.2719	1.0561	2.7865	3.8331
	D_z [10^{-9} C/m^2] ($\bar{z} = 0.5$ h)				
	−2.3798	−5.9665	−14.320	−40.978	−83.999
	$\mathcal{B}_z$ [10^{-7} T] ($\bar{z} = 0.5$ h)				
	1.3905	3.2990	7.7646	22.022	45.017

Table 14
Third new case in actuator configuration. Simply-supported multilayered (Adaptive Wood/0°/90°/0°/Adaptive Wood) spherical shell panel. $\Phi_t = 10$ V, $\Phi_b = 0$ V, $\Psi_t = 15$ A, $\Psi_b = 0$ A, $P_{z_t} = P_{z_b} = 0$ Pa. Imposed half-wave couples $m = n = 1$.

R_α/h	4	10	20	50	100
	w [10^{-9} m] ($\bar{z} = 0.5$ h)				
	7.6729	10.900	15.072	18.125	16.398
	ϕ [V] ($\bar{z} = 0.75$ h)				
	6.9360	7.8896	7.9704	7.8959	7.8704
	ψ [A] ($\bar{z} = 0.25$ h)				
	2.8893	3.2587	3.3171	3.3338	3.3362
	$\sigma_{\alpha\alpha}$ [10^{2} Pa] ($\bar{z} =$ h)				
	6.3867	4.2630	4.0528	4.3227	6.1342
	$\sigma_{\beta\beta}$ [10^{1} Pa] ($\bar{z} = 0$)				
	−3.3892	−12.344	−10.848	12.198	42.603
	σ_{zz} [10^{-2} Pa] ($\bar{z} = 0.5$ h)				
	196.89	−119.83	−118.13	−34.214	−9.3469
	D_z [10^{-11} C/m^2] ($\bar{z} = 0.5$ h)				
	−3.5905	−9.8447	−20.105	−50.621	−101.32
	$\mathcal{B}_z$ [10^{-6} T] ($\bar{z} = 0.5$ h)				
	−8.0879	−20.794	−41.782	−104.60	−209.24

model will consider material and geometrical nonlinearities in constitutive equations. Moreover, a full coupled thermo-electro-magneto-elastic 3D shell model will be developed via the proper addition of the 3D Fourier heat conduction equation.

CRediT authorship contribution statement

S. Brischetto: Writing – review & editing, Supervision, Methodology, Investigation, Formal analysis, Conceptualization. **D. Cesare:** Writing – original draft, Validation, Software, Investigation, Data curation. **T. Mondino:** Visualization, Validation, Software, Investigation, Data curation.

Declaration of competing interest

The authors declare that they have no known competing financial interests or personal relationships that could have appeared to influence the work reported in this paper.

Data availability

Data will be made available on request.

References

[1] Pan E, Heyliger PR. Free vibrations of simply supported and multilayered magneto-electro-elastic plates. J Sound Vib 2002;252:429–42.
[2] Ramirez F, Heyliger PR, Pan E. Free vibration response of two-dimensional magneto-electro-elastic laminated plates. J Sound Vib 2006;292(3–5):626–44.
[3] Razavi S, Shooshtari A. Nonlinear free vibration of magneto-electro-elastic rectangular plates. Compos Struct 2015;119:377–84.
[4] Wang Y, Xu R, Ding H, Chen J. Three-dimensional exact solutions for free vibrations of simply supported magneto-electro-elastic cylindrical panels. Internat J Engrg Sci 2010;48(12):1778–96.
[5] Vinyas M, Harursampath D. Nonlinear vibrations of magneto-electro-elastic doubly curved shells reinforced with carbon nanotubes. Compos Struct 2020;253:112749, 1-15.
[6] Vinyas M, Kattimani SC. Hygrothermal analysis of magneto-electro-elastic plate using 3D finite element analysis. Compos Struct 2017;180:617–37.
[7] Bhangale RK, Ganesan N. Static analysis of simply supported functionally graded and layered magneto-electro-elastic plates. Int J Solids Struct 2006;43(10):3230–52.
[8] Vinyas M. Computational analysis of smart magneto-electro-elastic materials and structures: review and classification. Arch Comput Methods Eng 2021;28:1205–48.
[9] Simões Moita JM, Mota Soares CM, Mota Soares CA. Analyses of magneto-electro-elastic plates using a higher order finite element model. Compos Struct 2009;91:421–6.
[10] Zhang P, Qi C, Fang H, Ma C, Huang Y. Semi-analytical analysis of static and dynamic responses for laminated magneto-electro-elastic plates. Compos Struct 2019;222:110933, 1-15.
[11] Zhou L, Gao Y. Mechanical-electro-magnetic coupling enriched finite element method for static analysis of magneto-electro-elastic composites. Mech Adv Mater Struct 2024;31(18):4374–86.
[12] Daga A, Ganesan N, Shankar K. Comparative studies of the transient response for PECP, MSCP, barium titanate, magneto-electro-elastic finite cylindrical shell under constant internal pressure using finite element method. Finite Elem Anal Des 2008;44:89–104.
[13] Li H, Zheng S, Shen Y, Han M, Zhang R, Zhao H. Hydro-steel structure digital twins: Application in structural health monitoring and maintenance of large-scale reservoir. Adv Eng Inform 2024;62:102922, 1-28.
[14] Wang Y, Zhu S, Wang B, Qin J, Qin G. Structural health monitoring of oil and gas pipelines: Developments, applications and future directions . Ocean Eng 2024;300:18293, 1-13.
[15] Wang L, Liu H, Zhang F, Guo L, Chen Z. Spatial structure digital twins: Application in intelligent health monitoring of cable dome structures. Autom Constr 2024;165:105489, 1-21.
[16] Pan E. Exact solution for simply supported and multilayered magneto-electro-elastic plates. J Appl Mech 2001;68(4):608–18.
[17] Pan E, Han F. Exact solution for functionally graded and layered magneto-electro-elastic plates. Internat J Engrg Sci 2005;43:321–39.
[18] Wang R, Han Q, Pan E. An analytical solution for a multilayered magneto-electro-elastic circular plate under simply supported lateral boundary conditions. Smart Mater Struct 2010;19:065025, 1-9.
[19] Milazzo A. Large deflection of magneto-electro-elastic laminated plates. Appl Math Model 2014;38:1737–52.
[20] Lage RG, Mota Soares CM, Mota Soares CA, Reddy JN. Layerwise partial mixed finite element analysis of magneto-electro-elastic plates. Comput Struct 2004;82:1293–301.
[21] Rao MN, Schmidt R, Schröder K-U. Geometrically nonlinear static FE-simulation of multilayered magneto-electro-elastic composite structures. Compos Struct 2015;127:120–31.
[22] Li M, Liu M, Zhou L. The static behaviors study of magneto-electro-elastic materials under hygrothermal environment with multi-physical cell-based smoothed finite element method. Compos Sci Technol 2020;193:108130, 1-19.
[23] Wu C-P, Chen S-J, Chiu K-H. Three-dimensional static behavior of functionally graded magneto-electro-elastic plates using the modified pagano method. Mech Res Commun 2010;37:54–60.
[24] She G-L, He Y-J. Nonlinear thermal buckling of magneto-electro-thermal-elastic plates with geometric imperfection. Struct Eng Mech 2025;93:115–23.
[25] Gan L-L, She G-L. Nonlinear combined resonance of magneto-electro-elastic plates. Eur J Mech A Solids 2025;109:105492, 1-17.
[26] Nixdorf TA, Pan E. Static plane-strain deformation of transversely isotropic magneto-electro-elastic and layered cylinders to general surface loads. Appl Math Model 2018;60:208–19.
[27] Chen JY, Pan E, Heyliger PR. Static deformation of a spherically anisotropic and multilayered magneto-electro-elastic hollow sphere. Int J Solids Struct 2015;60–61:66–74.
[28] Sobhy M. Magneto-electro-thermal bending of FG-graphene reinforced polymer doubly-curved shallow shells with piezoelectromagnetic faces. Compos Struct 2018;203:844–60.
[29] Arefi M, Amabili M. A comprehensive electro-magneto-elastic buckling and bending analyses of three-layered doubly curved nanoshell, based on nonlocal three-dimensional theory. Compos Struct 2021;257:113100, 1-18.
[30] Ye W, Liu J, Zang Q, Lin G. Investigation of bending behavior for laminated composite magneto-electro-elastic cylindrical shells subjected to mechanical or electric/magnetic loads. Comput Math Appl 2020;80:1839–57.
[31] Monge JC, Mantari JL, Llosa MN, Hinostroza MA. Unified layer-wise model for magneto-electric shells with complex geometry. Eng Anal Bound Elem 2024;163:33–55.
[32] Monge JC, Mantari JL, Hinostroza MA. Non-polynomial hybrid models for the bending of magneto-electro-elastic shells. Mech Adv Mater Struct 2024;31(17):4081–115.
[33] Song J, Wu D, Arefi M. Modified couple stress and thickness-stretching included formulation of a sandwich micro shell subjected to electro-magnetic load resting on elastic foundation. Def Technol 2022;18:1935–44.
[34] Mahesh V, Harursampath D. Nonlinear deflection analysis of CNT/magneto-electro-elastic smart shells under multi-physics loading. Mech Adv Mater Struct 2022;18:1935–44.
[35] Farajpour A, Rastgoo A. Size-dependent static stability of magneto-electro-elastic CNT/MT-based composite nanoshells under external electric and magnetic fields. Microsyst Technol 2017;23:5815–32.
[36] Albarody TMB, Al-Kayiem HH, Faris W. The transverse shear deformation behaviour of magneto-electro-elastic shell. J Mech Sci Technol 2016;30(1):77–87.
[37] Tornabene F, Viscoti M, Dimitri R. Magneto-electro-elastic analysis of doubly-curved shells: higher-order equivalent layer-wise formulation. Comput Model Eng Sci 2025;142(2):1768–838.
[38] Wu C-P, Tsai Y-H. Static behavior of functionally graded magneto-electro-elastic shells under electric displacement and magnetic flux. Internat J Engrg Sci 2007;45:744–69.
[39] Wu C-P, Chiu K-H, Wang Y-M. A mesh-free DRK-based collocation method for the coupled analysis of functionally graded magneto-electro-elastic shells and plates. Comput Model Eng Sci 2008;35(3):181–214.
[40] Cai Y, She G-L. Nonlinear dynamic response of magneto-electro-elastic cylindrical shells subjected to moving load. Mech Adv Mater Struct 2025;1–12.
[41] Gan L-L, She G-L. Nonlinear transient response of magneto-electro-elastic cylindrical shells with initial geometric imperfection. Appl Math Model 2024;132:166–86.
[42] Brischetto S. Exact three-dimensional static analysis of single- and multi-layered plates and shells. Compos Part B: Eng 2017;119:230–52.
[43] Brischetto S, Torre R, D. Cesare three dimensional coupling between elastic and thermal fields in the static analysis of multilayered composite shells. CMES - Comput Model Eng Sci 2023;136(3):2551–94.
[44] Brischetto S, Cesare D. 3D electro-elastic static analysis of advanced plates and shells. Int J Mech Sci 2024;280:109620, 1-29.
[45] Brischetto S, Cesare D. A 3D shell model for static and free vibration analysis of multilayered magneto-elastic structures. Thin-Walled Struct 2025;206:112620, 1-20.
[46] Hildebrand FB, Reissner E, Thomas GB. Notes on the foundations of the theory of small displacements of ortotropic shells. National Advisory Committee for Aeronautics Technical Note No. 1833, Washington, DC, USA: NACA; National Advisory Committee for Aeronautics; 1949.
[47] Povstenko Y. Fractional thermoelasticity. Cham, Switzerland: Springer International Publishing; 2015.
[48] Leissa A W. Vibration of shells. NASA SP-288, Washington, DC, USA; 1973.
[49] Tornabene F. Hygro-thermo-magneto-electro-elastic theory of anisotropic doubly-curved shells. Bologna (Italy): Società Editrice Esculapio; 2023.
[50] Monge JC, Mantari JL. Three dimensional numerical solution for the bending study of magneto-piezo-elastic spherical and cylindrical shells. Eng Struct 2021;238:112158, 1-19.
[51] Brischetto S. Convergence investigation for the exponential matrix and mathematical layers in the static analysis of multilayered composite structures. J Compos Sci 2017;1(2):19.
[52] Brischetto S. Convergence analysis of the exponential matrix method for the solution of 3D equilibrium equations for free vibration analysis of plates and shells. Compos Part B: Eng 2016;98:453–71.